Electromagnetic Thermoelectric Energy Harvesting Device

Hong-Ren Lin

A dissertation

submitted in partial fulfillment of the

requirements for the degree of

Doctor of Philosophy

University of Washington

2015

Reading Committee:

Wei-Chih Wang , Chair
Albert S. Kobayashi
Martin Afromowitz

Program Authorized to Offer Degree:

Mechanical Engineering

University of Washington

Abstract

Electromagnetic Thermoelectric Energy Harvesting Device

Hong-Ren Lin

Chair of the Supervisory Committee:
Dr. Wei-Chih Wang
Mechanical Engineering

The International Energy Agency (IEA) reports 17.6% annual growth rate in sustainable energy production. However, sustainable power generation based on environmental conditions (wind, solar) requires an infrastructure that can handle intermittent power generation. This dissertation proposes an electromagnetic thermoelectric (EMTE) device to overcome the intermittency problems of current sustainable energy technologies, providing the continuous energy supply unachievable by photovoltaic cells and portability impossible for traditional thermal electric (TE) generators. The EMTE converts environmental electromagnetic waves to a voltage output without requiring additional energy source. A single cell of this thermoelectric-inspired broadband EMTE can generate a 19.50 nV output within a 7.2 μm square area, with a verified linear scalability of the output voltage through cell addition. This idea leads to a challenge: the electrical polarity of each row of cells is the same but may require additional routing to combine output from each row. An innovative layout is proposed to overcome this issue through

switching the electrical polarity every other row. In this scheme, the EM wave absorption spectrum is not altered, and a simple series connection can be implemented to boost the total voltage output by one order within a limited area. To further improve the output over single cell, a passive EM wave intensity booster is tested. An 11.9 % voltage improvement is realized through an external 2D-grating structure. In the future, we expect to improve the performance in three different directions: first, incorporation of new materials; second, optimization of single cells; third, use of active intensity booster.

TABLE OF CONTENTS

List of Figures iii

List of Tables vii

Chapter 1. BACKGROUND 1

1.1 Sustainable Energy Roadmap 1

1.2 Energy from Environment 2

Chapter 2. INTRODUCTION 4

2.1 Electromagnetic Energy Absorption 4

2.2 Current Thermoelectric Technology 7

2.3 Motivation 8

2.4 Electromagnetic Wave Boosting Device 9

2.5 Overview 11

Chapter 3. FINITE DIFFERENCE TIME DOMAIN METHOD 14

3.1 Application of Numerical Methods 14

3.2 Yee's Formulation Of Maxwell's Equation 14

3.3 Perfect Matched Layer (PML) Boundary Condition 17

Chapter 4. ELECTROMAGNETIC ENERGY HARVESTING 20

4.1 Electromagnetic Absorber 20

4.1.1 Electromagnetic Material Properties: Permittivity and Permeability 20

4.1.2 Energy Absorber Design 22

4.1.3 Energy Dissipation over Absorber 29

4.2 Heat Conduction and Temperature Field 33

4.3 Thermoelectric Voltage 37

4.4 Energy Harvesting Array Design 38

4.5 Energy Harvesting Cell Design Layout Improvement 42

Chapter 5. EXTERNAL PASSIVE INTENSITY BOOSTER 45

Chapter 6. CONCLUSION 55

Chapter 7. FUTURE WORK 57

7.1 Material Research 57

7.2 Single Cell Design Topology 58

7.3 Development of External Devices 58

7.4 Fabrication Process 60

Bibliography 67

Appendix A 71

Appendix B 75

LIST OF FIGURES

Figure 1.1 US GSWO Annual Production [2]. 2
Figure 2.1 (a) A silver nanoparticle is placed at the interface of air and silica. The EM wave is traveling in the negative z direction and the electric field is pointing in the x direction (E_x). (b) The E_x is plotted over the central xz observation plane. (c) The E_x field is enlarged to visualize the concentration of the EM field. The diameter of the sphere is 96 nm and the incident wavelength is 394 nm. 4
Figure 2.2 Carnot efficiency vs. T_H temperature. 6
Figure 2.3 Application scenario of energy harvesting devices. 6
Figure 2.4 Power density spectrum of a 373 K body (orange solid), 300 K body (red dotted) and 273 K body (blue dashed). 9
Figure 2.5 Light focusing by convex lens. 10
Figure 2.6 The E_y magnitude of a s-polarization wave passing through a 1D grating at 30 THz. The observation xz plane is cut at the center of simulation domain and the y-direction is normal to the observation plane. 10
Figure 2.7 The workflow of the energy absorber design. 12
Figure 2.8 Content of this research. 13
Figure 3.1 Yee's E-field and H-field spatial grid assignment [30]. 16
Figure 3.2 Example of excitation signal waveform. 18
Figure 3.3 Hexahedral meshing of FDTD. 19
Figure 4.1 Square lattice distribution for simulation of the energy absorber. 23
Figure 4.2 Top view of different designs. 24
Figure 4.3 Skin depth of gold as a function of frequency. 25
Figure 4.4 Power absorption, reflection and transmission of Jeruselum cross absorber: the red line, blue line and blue dashed line stand for power absorption, transmission and reflection, respectively. 25

Figure 4.5 Power absorption, reflection and transmission of circular loop absorber: the red line, blue line and blue dashed line stand for power absorption, transmission and reflection, respectively. 26
Figure 4.6 Power absorption, reflection and transmission of fishnet absorber: the red line, blue line and blue dashed line stand for power absorption, transmission and reflection, respectively. 26
Figure 4.7 Power absorption, reflection and transmission circular patch absorber: the red line, blue line and blue dashed line stand for power absorption, transmission and reflection, respectively. 27
Figure 4.8 Power absorption, reflection and transmission of circular loop 2 absorber: the red line, blue line and blue dashed line stand for power absorption, transmission and reflection, respectively. 27
Figure 4.9 Top view of spiral design with dimensions L = 7.2 μm and w = 0.32 μm. Left arm is chromium and right arm is nickel. 28
Figure 4.10 Power absorption, reflection and transmission of the spiral absorber: the red line, blue line and blue dashed line stand for power absorption, transmission and reflection, respectively. 29
Figure 4.11 Electromagnetic energy dissipation over Jerusalem cross. 30
Figure 4.12 Electromagnetic energy dissipation over circular loop. 30
Figure 4.13 Electromagnetic energy dissipation over fishnet. 31
Figure 4.14 Electromagnetic energy dissipation over circular patch. 31
Figure 4.15 Electromagnetic energy dissipation over circular loop 2. 32
Figure 4.16 Electromagnetic energy dissipation over spiral. 32
Figure 4.17 Temperature field over Jerusalem cross. 34
Figure 4.18 Temperature field over circular loop. 35
Figure 4.19 Temperature field over fishnet design. 35
Figure 4.20 Temperature field over circular patch. 36
Figure 4.21 Temperature field over circular loop 2 design. 36
Figure 4.22 Temperature field over spiral design. 37

Figure 4.23 Temperature distribution over single spiral under normal incident 30 THz EM wave. 38
Figure 4.24 Energy dissipation distribution of an 11-by-11 spiral array. 40
Figure 4.25 Temperature distribution of an 11-by-11 spiral array. 40
Figure 4.26 Voltage output of single spiral under normal incident at 30 THz. 41
Figure 4.27 Voltage output of a 5-by-5 spiral array under normal incident at 30 THz. .. 41
Figure 4.28 Voltage output of an 11-by-11 spiral under normal incident at 30 THz. 41
Figure 4.29 Averaged voltage output versus array dimension. 42
Figure 4.30 Proposed electrical rout to switch electric polarity of every other row..... 43
Figure 4.31 S-parameter comparison of original and proposed (updated) designs. 43
Figure 4.32 Voltage output of revised 11-by-11 spiral array under normal incident 30 THz EM wave. 44
Figure 5.1 One example of gratings: L = 100 μm, a = 14.14 μm and b = 4.71 μm..... 45
Figure 5.2 The E_y amplitude distribution of a s-polarization wave at 30 THz passing through a structure in Figure 5.1. The observation xz plane is cut at the center of the simulation domain..... 46
Figure 5.3 E_y distribution of a s-polarization wave at 30 THz. The observation yz plane is cut at the center of simulation domain: (a) without EMTE; (b) with EMTE. 47
Figure 5.4 Energy dissipation pattern of a single EMTE cell from a 30 THz EM wave passing through a diffraction grating in Figure 5.1..... 48
Figure 5.5 Temperature field of single cell after 1D grating device..... 48
Figure 5.6 The design of 2D grating for a 30 THz incident EM wave (Front View). 49
Figure 5.7 P_z magnitude on xy plane 2.0 wavelengths away from 2D grating at 30 THz.50
Figure 5.8 A front view of the 2D grating with an observation line drawn..... 50
Figure 5.9 The intensity profile along the specified observation line shown in Figure 5.8.51
Figure 5.10 The alignment of EMTE single cell and 2D grating intensity booster..... 51
Figure 5.11 Temperature field distribution of a single spiral cell after a 30 THz wave passes through a 2D diffraction pattern. 52
Figure 5.12 Poynting vectors upon the EMTE single cell after a 30 THz wave is passing through a 2D diffraction grating as shown in Figure 5.10. 53

Figure 5.13 The EMTE shifts by 6 μm to positive x direction. (a) The plot shows the top view; (b) the plot shows the temperature distribution. 53
Figure 5.14 Voltage output of single EMTE spiral after a 30 THz wave is passed through a 2D diffraction grating as shown in Figure 5.10. 54
Figure 7.1 Top view of a case of planar gradient (10-by-10) device. The top and bottom electrodes are hidden for visualizing tuning conditions. Each color corresponds to the dielectric constant in Table 7.1. 59
Figure 7.2 E-field (absolute value) over a planar gradient device at 0.91 THz normal incidence. 60
Figure 7.3 Potential fabrication processes. 61
Figure 7.4 SEM image of a 20-nm line array after nickel lift-off and reactive ion etching (RIE). It was developed in pure IPA assisted by ultrasound agitation [58]. 61
Figure 7.5 SEM of focusing sub-wavelength gratin coupler. (a) top view; (b) sidewall view [59]. 62
Figure 7.6 Mold creation process flow. 63
Figure 7.7 The pattern transferring by silicon mold. 65
Figure 7.8 A CMOS structure example: TSMC 2P4M process 66
Figure 7.9 The reverse chip by CMOS post-processing. 66

LIST OF TABLES

Table 1.1. Summary of Energy Sources in A Typical Residential and Commercial Building [4] 2
Table 4.1. Table of Geometric Parameters (unit: μm) 24
Table 4.2. Q-factors of Different Designs 29
Table 4.3. Intensity versus Temperature 33
Table 7.1. Listing of The Material Properties in Figure 7.1. 59
Table 7.2. Structural Dimensions of Fully-etched Sub-wavelength Grating 62
Table 7.3. E-beam Lithography Recipe. 63
Table 7.4. Dry Etching Recipe. 64

ACKNOWLEDGEMENTS

I want to thank Professor Wang for showing me the research opportunity in University of Washington. I couldn't reach the goal of my research without his mentoring. I also appreciate the time we worked together to solve the difficulties and challenges.

This dissertation cannot be completed without the advices from the great advisory committee. I want to thank Professor Albert S. Kobayashi, Professor Martin Afromowitz and Professor Brian Nelson for their precious comments over this dissertation.

I want to express my appreciation to our group members: Chi Leung (Addison) Tsui for the hardware and software support; David Schipf for the research discussion; Ben Estroff for the paper discussion and comments; Gary, Jacob and George for the preparation of final defense.

I also want to thank the fellows who have supported me through these years: Jack Yang for all kinds of help and caring; Tim Liao for every discussion on electromagnetic wave theory and numerical methods.

Finally, I want to dedicate the achievement to my parents and brother. Their continuous encouragement and support is the source of power that keeps me up to the last step.

Chapter 1. BACKGROUND

1.1 SUSTAINABLE ENERGY ROADMAP

According to the UN report “Sustainable development is development that meets the needs of the present without compromising the ability of future generations to meet their own needs [1].” As economies of new developing countries grow, the demand for new energy supply is greater than ever. According to a report from the International Energy Agency (IEA), combustible fuel supplied more than 60% of required energy for members of Organization for Economic Cooperation and Development (OECD), while nuclear energy supplied 18% in 2012 [2]. In the European Union’s energy roadmap 2050 proposal, the dependence on fossil fuels and emission of carbon dioxide shall be reduced by at least 80% by 2050 [3]. Nuclear energy was considered as one option during the transition period. However, the Fukushima nuclear disaster in 2011 astonished the world and governments worldwide started nuclear energy policy amendment. In the long term, alternative renewable energy sources present solutions to meet the needs of the current generation without sacrificing the environment for the next generation. Energy generation with less environmental impact must be developed to offset the percentage of fossil fuel and nuclear sources. In IEA’s report, the annual growth rate of renewable energy was 17.6%. However, renewable energy occupied only 6% of the total energy consumption in 2013 [2]. This percentage implies room for renewable energy development. An upward trend in geo-thermal, solar, wind and other (GSWO) energy has been discovered in the US.

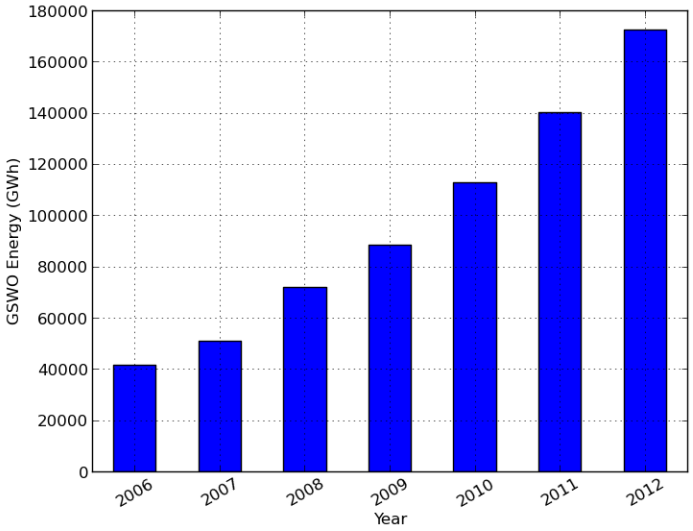

Figure 1.1 US GSWO Annual Production [2].

1.2 ENERGY FROM ENVIRONMENT

Collecting energy from surrounding environments is possible. Photovoltaic, thermoelectric, piezoelectric, radio frequency (RF) and airflow have been surveyed and evaluated for inside-building collection Table 1.1. Each technology has distinct advantages and disadvantages. For example, photovoltaic provides median power output but is restricted to the seasonal shift of sun light. Regional regulation or user requirements might set boundaries on this technology. In the survey, thermoelectric devices provide the greatest power output density. Yet it is limited by available indoor heat sources.

Table 1.1. Summary of Energy Sources in A Typical Residential and Commercial Building [4]

Harvester Type	Estimated Electrical DC Power	*Calculated Power Density
Photovoltaic	25 to 1149 μW	9 to 399 μW cm^{-3}
Thermal	1 to 10 mW	0.7 to 7.1 mW cm^{-3}
Periodic kinetic	0.008 to 68.97 μW	0.05 to 459.8 μW cm^{-3}
Electromagnetic wave	0.028 to 944 nW	1.69×10^{-3} to 57.37 nW cm^{-3}
Airflow	0.9 to 324 mW	1.7×10^{-2} to 6.0 mW cm^{-3}

* Calculated Power Density = Estimated electrical DC power divided by the volume of devices.

Well-tailored direct conversion of RF electromagnetic (EM) waves to DC is highly efficient. This idea can be traced back to 1969 [5]. It utilized the electron current resonance over a well-designed antenna array. The resonating current caused by EM waves is transformed into DC power through rectifiers. Another similar idea of strong magnetic resonance was recently applied in wireless power transfer [6]. But these two inventions focus on *power transfer* instead of *power generation*. External artificial energy sources are required, for example, in EM wave emitters.

At high operation frequencies, power generation by a device with feature sizes less than 10 μm has been made possible [7] due to the emerging nanotechnology. With appropriately designed resonators, continuous and efficient absorption of radiation becomes feasible. The development of metamaterial absorbers is the best example. Recently, these absorbers have proven the concept of *high absorption* [8, 9]. If highly absorptive cells are integrated with existing technologies—such as photovoltaic or thermoelectric—better sustainable energy sources can be expected.

Chapter 2. INTRODUCTION

2.1 ELECTROMAGNETIC ENERGY ABSORPTION

There are several options for collecting electromagnetic energy. The photovoltaic technology has been pursued and applied. Several techniques to improve conversion efficiency have been suggested. For example, surface plasmonics tailored by nanoparticles has seen some success. If nano-particles are embedded into dielectric substrate, the surface plasmon is able to concentrate the incident wave around the metal/dielectric interface [10, 11]. Figure 2.1 demonstrates such an effect of a silver spherical nano-particle over silica. Uniformity of nanoparticle clusters and periodic dispersion of nanoparticles is required for such a purpose. However, both tasks need more improvement. It requires some effort to disperse nanoparticles uniformly over a device, which is an important condition to provide desired field distribution [12, 13].

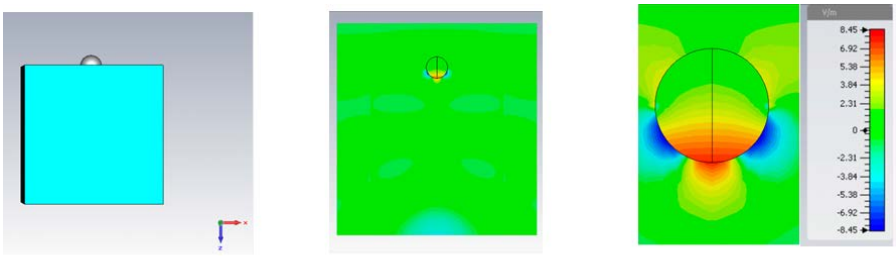

Figure 2.1 (a) A silver nanoparticle is placed at the interface of air and silica. The EM wave is traveling in the negative z direction and the electric field is pointing in the x direction (E_x). (b) The E_x is plotted over the central xz observation plane. (c) The E_x field is enlarged to visualize the concentration of the EM field. The diameter of the sphere is 96 nm and the incident wavelength is 394 nm.

Besides surface plasmons between dissimilar materials, surface waves induced by periodic metamaterial structures have been reported to increase the solar cell absorption [14]. The metamaterials become more feasible due to modern micro- and nano-fabrication techniques. They can improve existing photovoltaic technology by trapping more energy or they can be modified and become alternative energy sources.

Excitation of surface waves over periodic structures cannot complete the energy harvesting function. An additional conversion mechanism is required to convert absorbed energy. Assuming one conversion mechanism is integrated within an energy absorber, the total conversion efficiency η_{tot} can be expressed as a combination of three terms: the absorption efficiency of the absorber (η_a), conversion efficiency (η_c) and the last efficiency related to the loading element (η_l).

$$\eta_{tot} = \eta_a \eta_c \eta_l \tag{2-1}$$

In a photovoltaic cell, the first two terms can be combined into a single term to describe the conversion efficiency of a pure solar cell. For metal/insulator/metal (MIM) antenna rectifiers, a more delicate model [15, 16] is introduced but not applicable in this research.

Among the three terms, efficiency η_c depends on the conversion mechanism, while the loading element efficiency η_l depends on terminal loading as well as the intrinsic impedance of energy source itself. Since the loading is to be determined, the detailed discussion of η_l is not included in this research.

Thermoelectric conversion is adopted in this research. To estimate an upper bound of η_c, Carnot cycle efficiency may be applied. The equation is given by

$$\eta_c = 1 - \frac{T_c}{T_H}. \tag{2-2}$$

T_H and T_C are the temperatures of the hot source and the cold service end, respectively. Given the application scenario, the operation temperature of the device is supposed to be 298 K. The efficiency corresponding to various T_H is plotted in Figure 2.2.

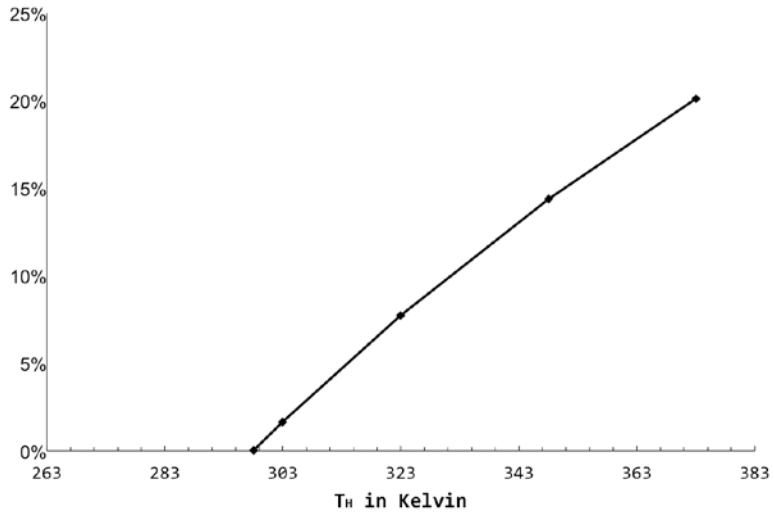

Figure 2.2 Carnot efficiency vs. T_H temperature.

As for the absorber efficiency η_a, high absorption nearly 100% have been reported in radio waves [17] and optical frequencies [16]. Our case is similar to these examples but focusing on improving η_a in the Long Wavelength Infrared region.

Some of the targeted radiation energy include heat emitted from human body, boiling water and various electronic appliances as shown in Figure 2.3. An initial assumption states the temperature of energy sources is between 0 ºC and 100 ºC. According to Wien's displacement law [18], temperature in this range shows a peak radiation around 10 μm, which corresponds to 30 THz.

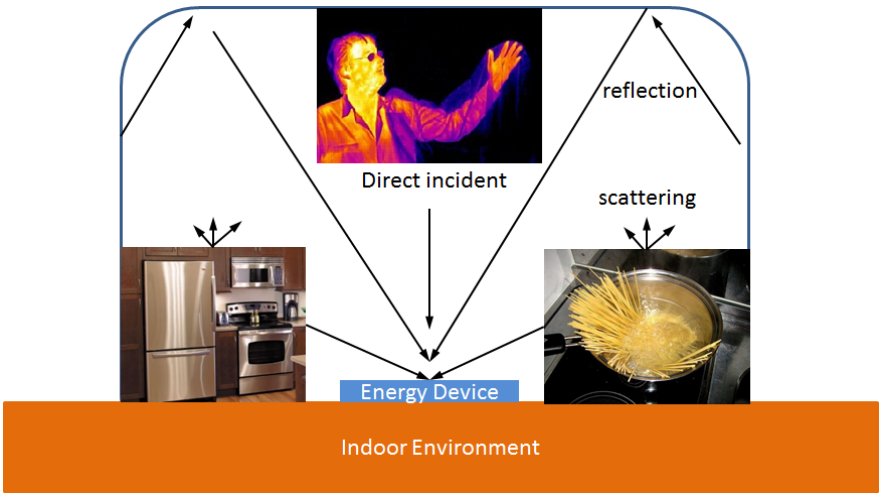

Figure 2.3 Application scenario of energy harvesting devices.

One of the attractions of using 10 μm wavelengths is its relatively high environmental transparency (low absorption). At wavelengths longer than 14 μm, CO_2 and CH_4 have high

absorption due to long C-H and carbonyl bonds and high H_20 absorption in rotational modes. At wavelengths shorter than 8 μm, H_2O and NH_3 absorb thermal infrared radiation. In between 8 μm and 14 μm, only ozone has high absorption which contains only small percentage of the atmospheric composition [19]. In other words, 30 THz EM waves have long traveling distance due to relatively low absorption.

2.2 CURRENT THERMOELECTRIC TECHNOLOGY

The Seebeck effect was discovered over a closed loop composed of two dissimilar metals [20]. When a temperature gradient exists over the metals, an electrical potential is triggered. To quantify the relation between temperature difference and generated electric potential, the Seebeck coefficient S is defined as

$$S = \frac{\Delta V}{\Delta T}. \tag{2-3}$$

ΔV is the generated electric potential difference and ΔT is the temperature difference between two terminals of conjugated dissimilar metals. This equation implies a positive Seebeck coefficient when the potential gradient has the same direction as the temperature gradient.

Famous thermoelectric applications include bi-metal thermal couples and thermoelectric generators (TEGs) [21]. Some TEGs consist of n-type and p-type semiconductors of which the thermal conductivity, electrical conductivity, Seebeck coefficients S and dimensional parameters can be tuned to maximize either the efficiency or output power. An example is found in matching of thermal conductance and electrical resistance for the figure of merit optimization [22].

Micro TEG has been attempted to use the advantages of micro-fabrication with thermoelectric materials. A well-known example is the power generating for wrist watches reported in 1999 [23]. Various bulk micromachining [24] and CMOS-compatible processes [25] have been attempted to shrink the size and improve the performance of TE generators. A 67 μV at 1 K temperature difference was reported on the mentioned CMOS-MEMS TE generator [25]. However, these generators must be attached to heat sources. The electric modeling is also limited to the conduction-type TE generator [26].

It is noted that single TEG provides limited voltage output. To satisfy real application scenarios, traditional TEGs normally adopt serial connections to boost voltage output [23, 24, 26, 27].

For bi-metal designs, only the material properties of two materials are under consideration. They include thermal conductivity, electrical conductivity and Seebeck coefficients. To maximize voltage generation between two conductors, the temperature distribution has to be optimized. The temperature field analysis cannot be resolved without thermal analysis.

2.3 MOTIVATION

Our living space is full of radiative energy sources. Examples include radiators, electronics, cars and the human body. These energy sources randomly radiate electromagnetic waves into the environment. With appropriate devices, the energy can be collected. Take the human body as an example. The temperature distribution and the corresponding radiative heat rate is evaluated in a literature [28]. The mean radiant temperature is around 27 ℃, or 300 K. The power density spectrum of a 300 K object can be quickly estimated by Planck's law as plotted on Figure 2.4. The equation for Planck's Law is

$$B_\lambda(T) = \frac{2hc^2}{\lambda^5}\frac{1}{e^{\frac{hc}{\lambda k_B T}}-1}. \tag{2-4}$$

where h is the Planck constant, k_B is the Boltzmann constant, c is the speed of light, λ is the wavelength and T is the absolute temperature. Two additional curves with temperatures 273 K and 373 K are also plotted in Figure 2.4 for comparison.

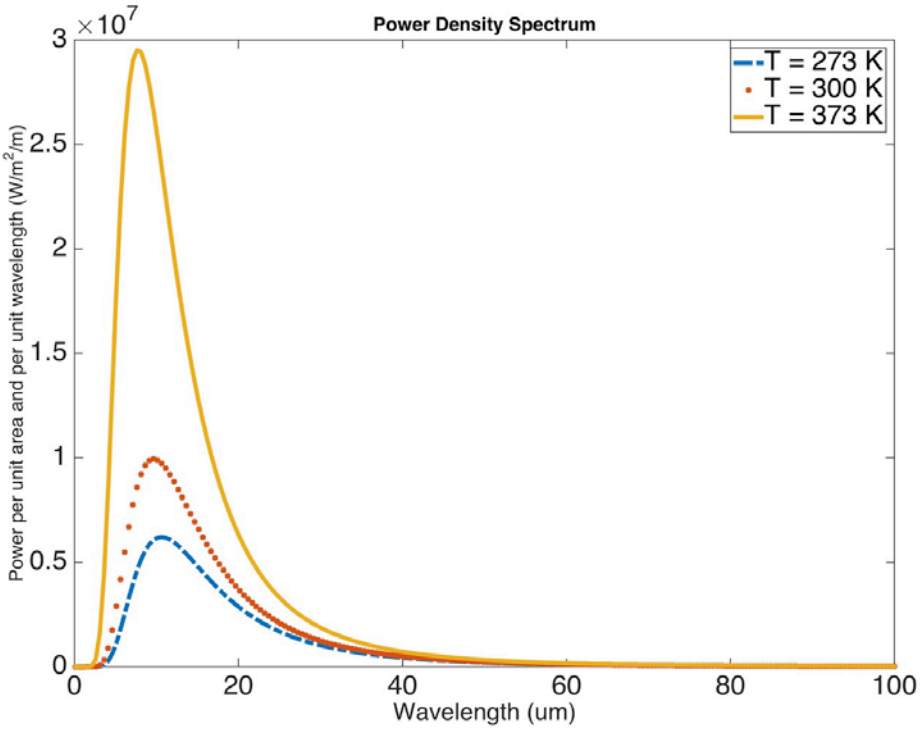

Figure 2.4 Power density spectrum of a 373 K body (orange solid), 300 K body (red dotted) and 273 K body (blue dashed).

From Figure 2.4, it is seen that the peak value of power density is at a wavelength of ~10 μm, which corresponds to 30 THz. To make use of this radiation in our environment, a novel device is proposed to absorb energy at this frequency and thermoelectric design is embedded into this device to convert the absorbed energy.

2.4 Electromagnetic Wave Boosting Device

Besides device level improvement, additional devices could manipulate the spatial distribution of incident wave. This concept is similar to convex lens that focuses light.

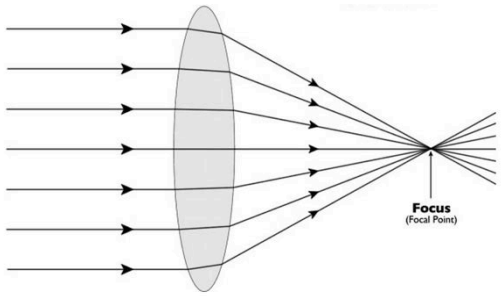

Figure 2.5 Light focusing by convex lens[1].

Fortunately, recent developments in optical devices provide useful examples for energy devices. For example, periodic slits can distribute the light into certain directions. One example, shown in Figure 2.6, demonstrates the scattered pattern of a plane wave passing through periodic slits (grating). This scattered pattern is expected to excite interesting effect over space-sensitive devices, for example, solar cells or thermoelectric generators.

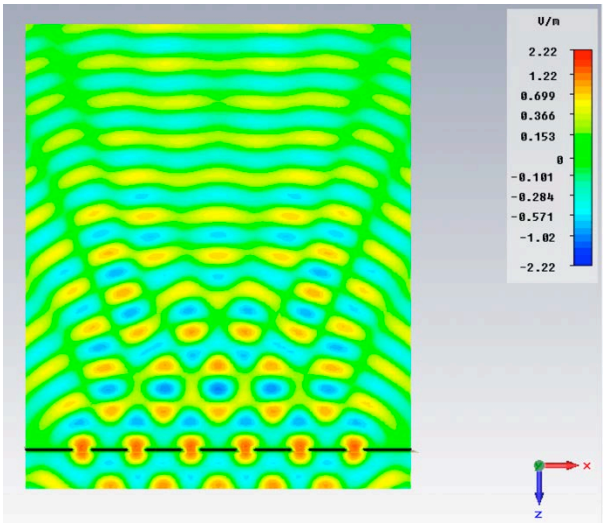

Figure 2.6 The E_y magnitude of a s-polarization wave passing through a 1D grating at 30 THz. The observation xz plane is cut at the center of simulation domain and the y-direction is normal to the observation plane.

[1] https://www.luxexcel.com/custom-optics/lens-types-explained/

2.5 OVERVIEW

A general background review was given in the first chapter of this dissertation. The purpose is to explain the global trend of renewable energy. From the EU proposal and IEA data, it can be seen that the requirement growth of renewable energy is strong. Besides, indoor scale research shows the potential of different renewable technologies.

The second chapter introduces technologies involved in this integrative research. It is divided into three parts: electromagnetic energy absorption, thermoelectric conversion and wave boosting devices. The purpose is to review studies related to each topic.

Since the finite difference time domain (FDTD) method is the major technique to resolve the electromagnetic wave field in finite domains, it is worthy to discuss the basic formulation of this method. The formulation of Yee's cell and a perfect matching layer (PML) is covered in the third chapter.

The major focus of chapter four is the design of the energy absorber and thermoelectric energy generation. The electromagnetic absorber design is divided into preliminary single cell design and absorption optimization. In this part, a frequency domain solver and Floquet boundary conditions are applied. The purpose is to quickly build reasonable dimensions of a single cell. Once the geometric parameters of single cell are formulated, a time domain solver with a plane wave signal source is applied over a finite array to estimate the energy dissipation distribution over the whole structure. With the values of energy dissipation, thermal analysis follows up to estimate the temperature distribution over the structure. After the temperature field is available, the electric potential created by the Seebeck effect can be estimated. To increase the voltage output, the absorber geometry has to be tuned several times. This workflow is shown in Figure 2.7.

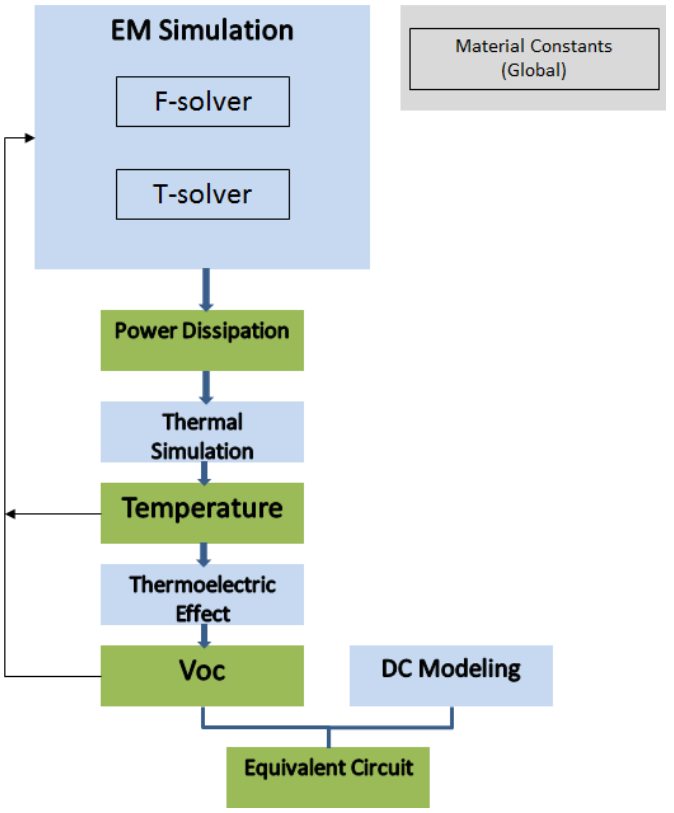

Figure 2.7 The workflow of the energy absorber design.

In addition to optimization of a single cell structure, another way to re-distribute energy over the single cell is through the use of an external device. In chapter five, the discussion lies on the incorporation of such an external device, by which the wave is scattered or focused onto a certain point.

In chapter six, we conclude the results of this work. A broad-band device is created. By the incorporation of bi-metal spiral, the energy concentration is obvious. This concentration creates a favored temperature gradient that prompts thermoelectric voltage. Through the modification of the design layout, the connection of each single cell is improved. To further enhance the energy concentration, one passive grating is introduced to modulate the temperature field over energy harvesting cell.

In chapter seven, it is predicted that the incorporation of new material could probably enhance the output but manufacturing compatibility requires more tests. As for the design, single cells that concentrate energy at one point are worth more investigation. To make the distribution of energy dissipation more asymmetric, an external device such as a convex lens may be helpful.

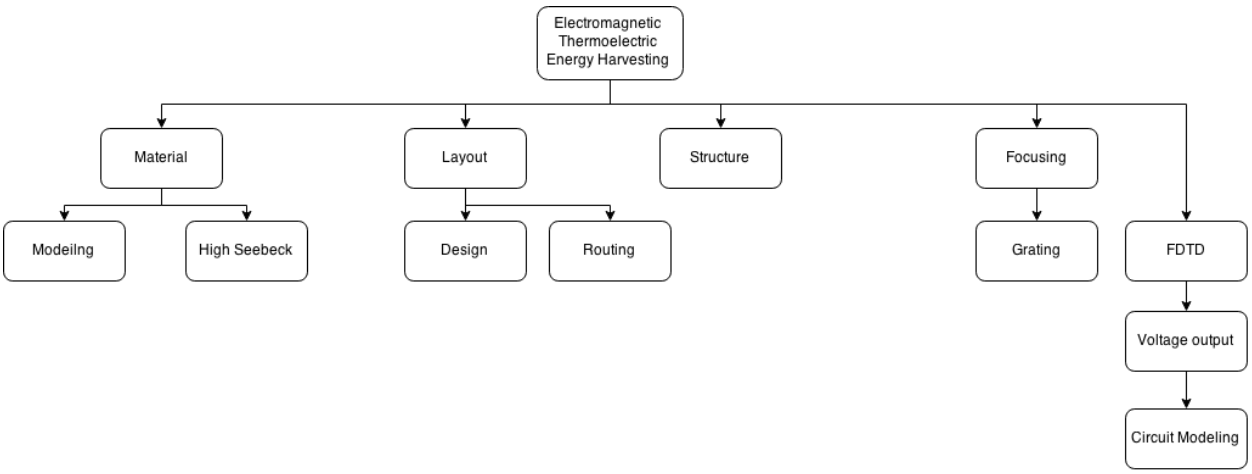

Figure 2.8 Content of this research.

Chapter 3. FINITE DIFFERENCE TIME DOMAIN METHOD

3.1 APPLICATION OF NUMERICAL METHODS

Analytical solutions for wave propagation are possible for simple and symmetric structures. In most of cases, real structure geometry makes it challenging to derive a complete solution. As a result, numerical methods are needed. The finite difference time domain (FDTD) method is applicable for electrically large devices and able to provide the solutions near sample boundaries. Such solutions can help the understanding of the boundary effect over the device performance. This chapter discusses the fundamentals of FDTD formulation especially in EM wave propagation.

3.2 YEE'S FORMULATION OF MAXWELL'S EQUATION

Maxwell's equations are the standard for electromagnetic problems. In a macroscopic view of materials, these equations are eminent tools to understand the effects of materials types and material properties on given problems. The starting point is the differential form of Maxwell's equations [29].

$$\begin{aligned} \nabla \cdot \vec{D} &= \rho \\ \nabla \cdot \vec{B} &= 0 \\ \nabla \times \vec{E} &= -\frac{\partial \vec{B}}{\partial t} \\ \nabla \times \vec{H} &= \frac{\partial \vec{D}}{\partial t} + \vec{J} \end{aligned} \tag{3-1}$$

where $\vec{E}$: electric field;

$\vec{H}$: magnetic field;

$\vec{D}$: electric displacement;

$\vec{B}$: magnetic flux density;

ρ : volumetric electric charge density;

$\vec{J}$: surface electric current density;

ϵ : permittivity;

μ : permeability;

σ : conductivity.

Instead of solving the complete set of Maxwell's equations, Yee's formulation starts from Faraday's law and Ampere's law. Though free electric current and magnetic current do not generally exist inside a simulation domain, the loss due to electric conductivity and magnetic conductivity shall be included for general purpose. The equations to be discretized are

$$\frac{\partial \vec{B}}{\partial t} = -\nabla \times \vec{E} - \sigma^* \vec{H} \tag{3-2}$$

$$\frac{\partial \vec{D}}{\partial t} = \nabla \times \vec{H} - \sigma \vec{E}, \tag{3-3}$$

where the additional σ^* is magnetic conductivity.

The electric displacement, magnetic flux density and electric current density are further expressed as

$$\vec{D} = \epsilon \vec{E} = \epsilon_r \epsilon_0 \vec{E} \tag{3-4}$$

$$\vec{B} = \mu \vec{H} = \mu_r \mu_0 \vec{H} \tag{3-5}$$

$$\vec{j} = \sigma \vec{E}, \tag{3-6}$$

where ε and μ are the permittivity and permeability of materials, ε_0 and μ_0 are the permittivity and permeability of free space, ε_r and μ_r are the relative permittivity and permeability. Substituting (3-4) and (3-5) into (3-2) and (3-3) we arrive at

$$\frac{\partial \vec{H}}{\partial t} = -\frac{1}{\mu} \nabla \times \vec{E} - \frac{1}{\mu} \sigma^* \vec{H} \tag{3-7}$$

$$\frac{\partial \vec{E}}{\partial t} = \frac{1}{\epsilon} \nabla \times \vec{H} - \frac{1}{\epsilon} \sigma \vec{E} \,. \tag{3-8}$$

If two vector equations above are expanded into their scalar components, we have

$$\frac{\partial H_x}{\partial t} = -\frac{1}{\mu} \left[\frac{\partial E_z}{\partial y} - \frac{\partial E_y}{\partial z} \right] - \frac{\sigma^*}{\mu} H_x \tag{3-9}$$

$$\frac{\partial H_y}{\partial t} = -\frac{1}{\mu} \left[\frac{\partial E_x}{\partial z} - \frac{\partial E_z}{\partial x} \right] - \frac{\sigma^*}{\mu} H_y \tag{3-10}$$

$$\frac{\partial H_z}{\partial t} = -\frac{1}{\mu}\left[\frac{\partial E_y}{\partial x} - \frac{\partial E_x}{\partial y}\right] - \frac{\sigma^*}{\mu} H_z \tag{3-11}$$

$$\frac{\partial E_x}{\partial t} = \frac{1}{\varepsilon}\left[\frac{\partial H_z}{\partial y} - \frac{\partial H_y}{\partial z}\right] - \frac{\sigma}{\varepsilon} E_x \tag{3-12}$$

$$\frac{\partial E_y}{\partial t} = \frac{1}{\varepsilon}\left[\frac{\partial H_x}{\partial z} - \frac{\partial H_z}{\partial x}\right] - \frac{\sigma}{\varepsilon} E_y \tag{3-13}$$

$$\frac{\partial E_z}{\partial t} = \frac{1}{\varepsilon}\left[\frac{\partial H_y}{\partial x} - \frac{\partial H_x}{\partial y}\right] - \frac{\sigma}{\varepsilon} E_z \tag{3-14}$$

These six equations are coupled partial differential equations and they are the basis for FDTD numerical formulation. Yee assigned grid points for this formulation as shown in Figure 3.1. The E-field components are in the middle of the edges and the H-field components are in the center of the faces.

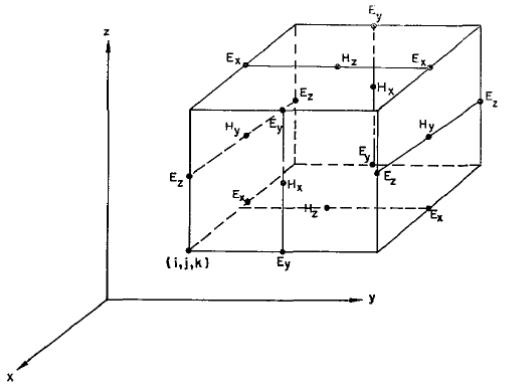

Figure 3.1 Yee's E-field and H-field spatial grid assignment [30].

After the spatial grid is determined, we can apply 2nd order central difference scheme with this grid. Consequently, (3-9) becomes the equation (3-15) given below. The rest of the equations can be derived following similar procedures [31].

$$H_x\left(i+\frac{1}{2},j,k\right)^{\left(n\Delta t+\frac{1}{2}\Delta t\right)} =$$

$$\frac{\frac{1}{\Delta t}-\frac{\sigma^*}{2\mu}}{\frac{1}{\Delta t}+\frac{\sigma^*}{2\mu}} H_x\left(i+\frac{1}{2},j,k\right)^{\left(n\Delta t-\frac{1}{2}\Delta t\right)}$$

$$-\frac{1}{\left(\frac{1}{\Delta t}+\frac{\sigma^*}{2\mu}\right)\mu\Delta y}\left[E_z\left(i+\frac{1}{2},j+\frac{1}{2},k\right)^{(n\Delta t)} - E_z\left(i+\frac{1}{2},j-\frac{1}{2},k\right)^{(n\Delta t)}\right]$$

$$+\frac{1}{\left(\frac{1}{\Delta t}+\frac{\sigma^*}{2\mu}\right)\mu\Delta z}\left[E_y\left(i+\frac{1}{2},j,k+\frac{1}{2}\right)^{(n\Delta t)} - E_y\left(i+\frac{1}{2},j,k-\frac{1}{2}\right)^{(n\Delta t)}\right].$$

(3-15)

Numerical stability is conserved if the time step (Δt) is properly defined. The time step Δt is determined by spatial steps in Cartesian coordinates Δx, Δy and Δz. For three dimensional Maxwell's equations, the Courant-Friedrich-Levy (CFL) stability condition is satisfied by

$$\Delta t \leq \Delta t_{max} = \frac{1}{c\sqrt{\frac{1}{\Delta x^2}+\frac{1}{\Delta y^2}+\frac{1}{\Delta z^2}}}. \tag{3-16}$$

To further simplify the problem, we can set equal spatial steps in three directions.

$$\Delta x = \Delta y = \Delta z = \Delta \tag{3-17}$$

Then, the time step is simplified to

$$\Delta t \leq \Delta t_{max} = \frac{\Delta}{c\sqrt{3}}. \tag{3-18}$$

3.3 Perfect Matched Layer (PML) Boundary Condition

The simulation domain is discretized according to a coordinate system. In any coordinate system, the simulation domain must be confined due to computer hardware limits. Boundaries to constrain dimensions of the simulation domain are thus required. A type of boundary often used in electromagnetic simulations is the perfect matched layer (PML) [32]. Inside the PML, each E-field component and H-field component from (3-9) to (3-14) is divided into two parts. With a matching condition given below as equation (3-19), the reflection is theoretically zero at a PML interface.

$$\frac{\sigma}{\epsilon} = \frac{\sigma^*}{\mu} \tag{3-19}$$

Gedney [33] proposed a uniaxial PML (UPML) which requires no division of E-field and H-field. The method starts by looking at the uniaxial medium and introduces additional steps to relate D-field, H-field and E-field as shown in (3-20) and (3-21).

Though more updating steps are required in UPML, it utilizes the original E-field and H-field and can be generalized to a lossy isotropic medium.

$$D_z\left(i,j,k+\frac{1}{2}\right)^{\left(n\Delta t+\frac{1}{2}\Delta t\right)} =$$

$$D_z\left(i,j,k+\frac{1}{2}\right)^{\left(n\Delta t-\frac{1}{2}\Delta t\right)}$$

$$+\Delta t\left(\frac{H_y\left(i+\frac{1}{2},j,k+\frac{1}{2}\right)^{(n\Delta t)}-H_y\left(i-\frac{1}{2},j,k+\frac{1}{2}\right)^{(n\Delta t)}}{\Delta x}-\frac{H_x\left(i,j+\frac{1}{2},k+\frac{1}{2}\right)^{(n\Delta t)}-H_x\left(i,j-\frac{1}{2},k+\frac{1}{2}\right)^{(n\Delta t)}}{\Delta y}\right).$$

(3-20)

$$E_z(i,j,k)^{\left(n\Delta t+\frac{1}{2}\Delta t\right)} =$$

$$E_z(i,j,k)^{\left(n\Delta t-\frac{1}{2}\Delta t\right)}$$

$$+\frac{1}{\varepsilon_0\varepsilon_r}\left(D_z(i,j,k)^{\left(n\Delta t+\frac{1}{2}\Delta t\right)}\left(1+\frac{\sigma\Delta t}{2\varepsilon_0}\right)-D_z(i,j,k)^{\left(n\Delta t-\frac{1}{2}\Delta t\right)}\left(1-\frac{\sigma\Delta t}{2\varepsilon_0}\right)\right).$$

(3-21)

With this formulation, electrically large and geometrically complicated structures can be simulated. Normally, a Gaussian cosine wave excitation signal is used, depending on the required frequency range. In addition, the structural meshing is generally hexahedral.

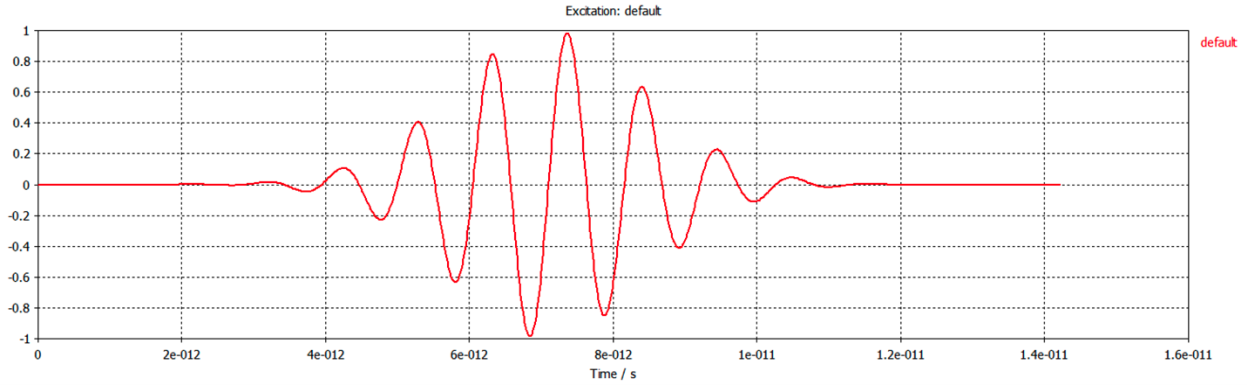

Figure 3.2 Example of excitation signal waveform.

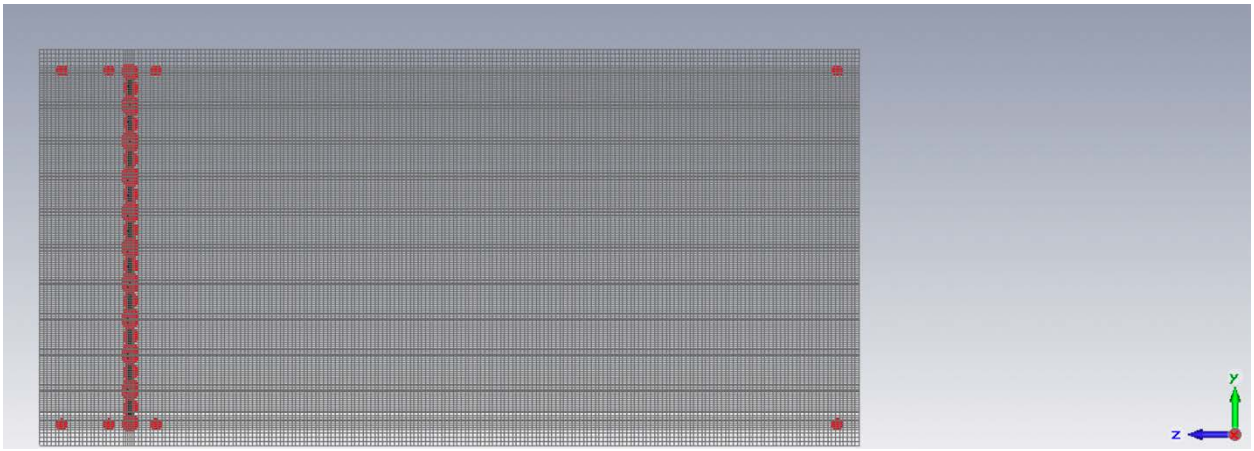

Figure 3.3 Hexahedral meshing of FDTD.

Chapter 4. ELECTROMAGNETIC ENERGY HARVESTING

4.1 ELECTROMAGNETIC ABSORBER

If not specifically noted, the physics notation of a traveling wave is adopted hereafter. The equation is given by

$$\vec{E} = \vec{E}_0 e^{i(\vec{k}\cdot\vec{r}-\omega t)} \tag{4-1}$$

The imaginary parts of permittivity, permeability and refractive index shall be expressed as a positive real numbers in the definition of passive and lossy materials when necessary.

It is assumed that no free charge or free current exists inside a dielectric material. Taking the curl of Faraday's law, the equation becomes

$$\nabla^2 \vec{E} = \mu\varepsilon \frac{\partial^2 \vec{E}}{\partial^2 t}. \tag{4-2}$$

Substituting (4-1) into (4-2) leads to

$$(k_x^2 + k_y^2 + k_z^2)\vec{E} = \omega^2 \mu\varepsilon\vec{E} \tag{4-3}$$

$$\left|\vec{k}\right| = \sqrt{k_x^2 + k_y^2 + k_z^2}\,, \tag{4-4}$$

which relates wave vectors with material properties.

Normally, the wave velocity inside a material can be written in terms of permittivity and permeability as

$$V_p = \sqrt{\mu\varepsilon}^{-1} = \sqrt{\mu_0\mu_r\epsilon_0\epsilon_r}^{-1} = \frac{c}{n}, \tag{4-5}$$

where *c* is speed of the EM wave in a vacuum and *n* is the refractive index of the material.

The eigenvalue equation (4-3) plays an important role in many problems. For example, the derivation of a surface plasmon, band gap structure of photonic crystals and periodic metamaterial [34] all utilize equation (4-3). In the following sections, Maxwell's equations will be cited either in the derivation of material properties or in the design of the absorber.

4.1.1 *Electromagnetic Material Properties: Permittivity and Permeability*

If not specifically noted, raw materials will be treated as isotropic and homogeneous. They include dielectric and conductive materials. In the absorber design, the dielectric material is to

support the whole structure, to create a distance between electrodes, and to prevent unnecessary heat transfer. SU-8 is such a dielectric material and widely used in many applications due to its chemical stability. Besides, sufficient material property data for SU-8 is available in wide frequency ranges, including those that support this research goal [35-37]. The material has also been tested in our previous THz metamaterial [38] .

In the derivation of material properties, Maxwell's equations are required. Several assumptions are adopted: first, there is no volumetric electric charge inside the structure; second, the conductor is homogeneous during operation; third, incident waves are not strong enough to change material properties. At GHz levels, conductive material properties are formulated in terms of one real permittivity and one loss tangent. Considering the conductivity, the curl of Faraday's Law becomes

$$\nabla^2\vec{E} = \mu\varepsilon\frac{\partial^2\vec{E}}{\partial^2 t} + \sigma\,\mu\frac{\partial\vec{E}}{\partial t} = \mu(-\omega^2\varepsilon - i\omega\sigma)\vec{E} \tag{4-6}$$

which is able to describe the complex permittivity of conductors at low frequency. It is clear the imaginary term originates from the conductivity, which leads to the "lossy" part of conductive material. When applying lossy conductors in modeling, meshing is not a significant issue for numerical analysis.

When operating at and above 30 THz, the Drude model is needed to describe the material properties. In some cases, the Drude model is sufficient for common metals (e.g. gold) [39]. For some rarely used metals such as chromium and nickel, the Drude-Lorentz model is needed as well to describe material properties at higher frequencies [40].

The use of electric conductors is important in our design. Besides scattering electromagnetic waves and creating necessary energy absorption, conductors provide an electrical conduction path. Since gold, chromium, nickel and other common metals will be used in our 30 THz device, the Drude model will be used.

Because materials in this research are not magnetic, the permeability $\mu = 1$ is considered. Permittivity values of the dielectric materials, including SU-8, are mostly collected from literature.

A silicon substrate is the supporting layer for the absorber design. It is not necessary to include the silicon layer in the simulation. The reason is that the supporting silicon is shielded by the bottom electrode. The advantage of ignoring the silicon layer in the simulation is the obvious lessening of computation complexity and memory space needed.

4.1.2 *Energy Absorber Design*

A single energy absorber is a 2D array composed of repeated single cells. It is sometimes mentioned as a "device" in this research. To absorb more energy, a very large 2D array is necessary. As a result, the design of single cell becomes an EM problem of periodic boundary conditions extended to infinity. The Bloch-Floquet theorem provides a recipe to formulate the solution as a periodic function.

$$U(\vec{r}) = U(\vec{r} + \vec{a}) \tag{4-7}$$

where $\vec{a}$ is a translation vector related to the periodicity of single cell.

A square lattice with equivalent periodicity on the device surface is adopted as shown in Figure 4.1. The lattice length (L) is related to operation wavelength (λ_0) as $\lambda_0 \sim 2L$ [41]. Under such a scheme, the solution can be formulated as

$$\mathrm{U}(\vec{\mathrm{r}}) = \sum_{\mathrm{m}=-\infty}^{\infty} \sum_{\mathrm{n}=-\infty}^{\infty} \mathrm{f_n(z)} \mathrm{e}^{\mathrm{i}(\alpha_\mathrm{m} \mathrm{x} + \beta_\mathrm{n} \mathrm{y})} \tag{4-8}$$

$$\alpha_\mathrm{m} = \alpha_0 + \mathrm{m} \frac{2\pi}{\mathrm{L}} \tag{4-9}$$

$$\beta_\mathrm{n} = \beta_0 + \mathrm{n} \frac{2\pi}{\mathrm{L}} \tag{4-10}$$

where α and β correspond to wave numbers in the x and y directions, respectively. With such formulation and appropriate boundary conditions, analytically deriving the amplitude function by Fourier transform is possible in simple designs. However, numerical methods, such as FDTD, are required for finite array analysis.

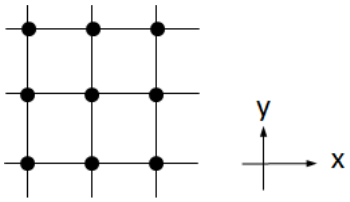

Figure 4.1 Square lattice distribution for simulation of the energy absorber.

Similar to surface plasmons, surface electromagnetic waves over the array surface are responsible for energy absorption. Another way to explain the high absorption is the electric and magnetic resonances over the periodic structure. When incident wave encounters the top electrode, electrons are driven back and forth over the top electrode. Since the electrodes are lossy, this resonating current introduces high power dissipation over this layer. This current is a function of excitation frequency, geometry and composing materials.

Some basic patterns, such as loop type, N-pole type, patch type and screen type follow a rule of thumb: the summation of single cell periphery is proportional to the target wavelength or frequency [42]. For example, the radius of a circular loop design is related to target frequency by

$$2\pi r = \lambda_t = \frac{c}{f_t} \qquad (4\text{-}11),$$

where r is the central radius of the circular loop, λ_t is the wavelength corresponding to target frequency f_t and c is the speed of light in free space, 3 x 10^8 m/s.

For different types of absorber designs, the geometric parameters need optimization due to fringe effects. Some design examples are shown in Figure 4.2, with the corresponding design parameters listed in Table 4.1. It is concluded that all these designs have narrow band features. However, the lattice distance and thickness of each design is different. This phenomenon hints that the different space efficiency of each design can be further related to the oscillating parameters [41]. In other words, if per unit area or per unit length of design is critical in an application, either the circular patch design or the circular loop 2 design are good options when compared to other designs as shown in Table 4.1.

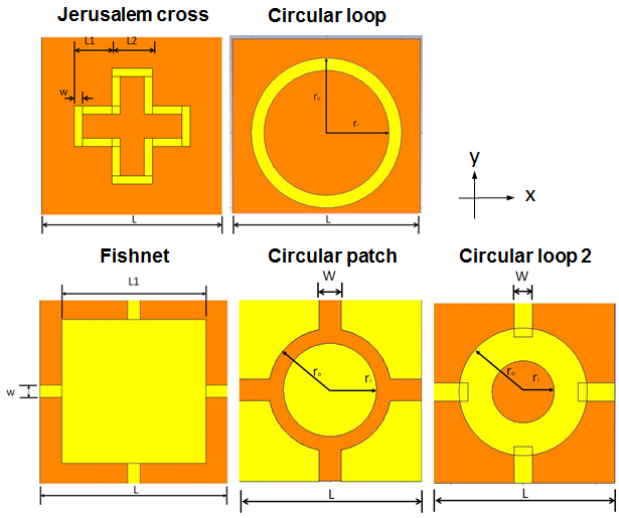

Figure 4.2 Top view of different designs.

Table 4.1. Table of Geometric Parameters (unit: μm)

	L	L1	L2	t_{sub}	t_e	W
Jerusalem cross	4.87	1.44	1.09	2.38	0.20	0.22
	L	r_i	r_o	t_{sub}	t_e	
Circular loop	5.1	1.52	1.85	2.48	0.20	
	L	L1		t_{sub}	t_e	W
Fishnet	4.48	3.00		2.52	0.20	1.31
	L	r_i	r_o	t_{sub}	t_e	W
Circular patch	5.50	1.33	1.80	1.68	0.20	0.14
	L	r_i	r_o	t_{sub}	t_e	W
Circular loop 2	3.80	1.07	1.50	2.55	0.20	1.13

The power absorption for the device given reflection and transmission is defined as [43]

$$A = 1 - R - T \tag{4-12}$$

where R and T are the amplitude squares of complex scattering parameters S11 and S21, respectively. At 30 THz, a 200 nm thick gold plate is much thicker than the corresponding skin depth, which is evaluated as

$$\delta = \sqrt{\frac{2\rho}{\omega\mu}}. \tag{4-13}$$

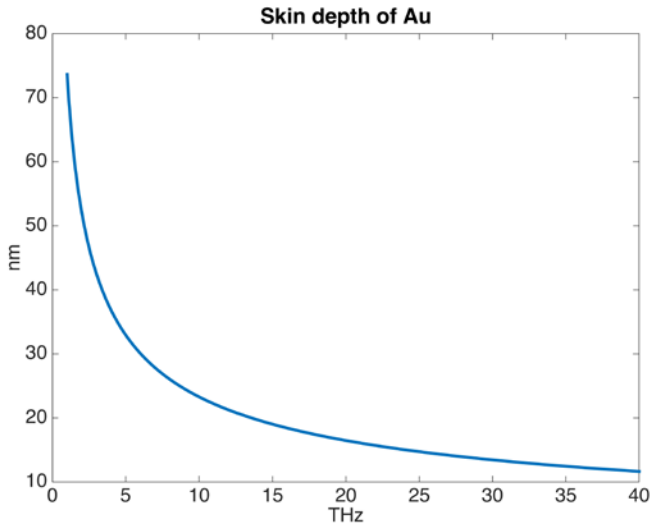

Figure 4.3 Skin depth of gold as a function of frequency.

A single cell backed by a full block of bottom gold shall not have transmission due to the thick gold layer. It also means the absorption is mainly affected by the reflection in (4-12). The following graphs demonstrate the transmission, reflection and absorption of each design listed in Table 4.1.

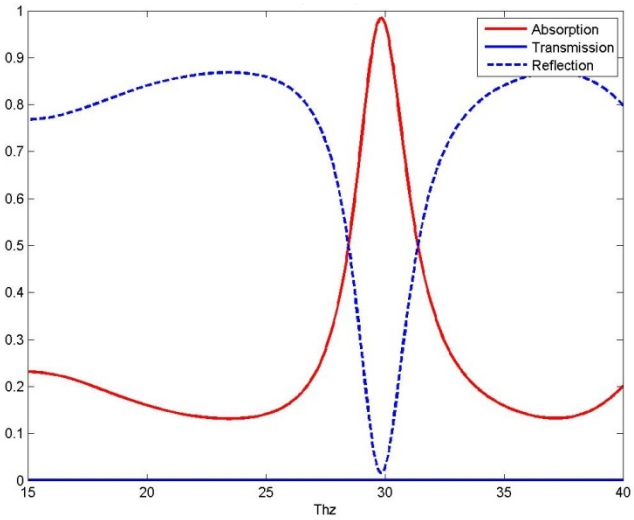

Figure 4.4 Power absorption, reflection and transmission of Jeruselum cross absorber: the red line, blue line and blue dashed line stand for power absorption, transmission and reflection, respectively.

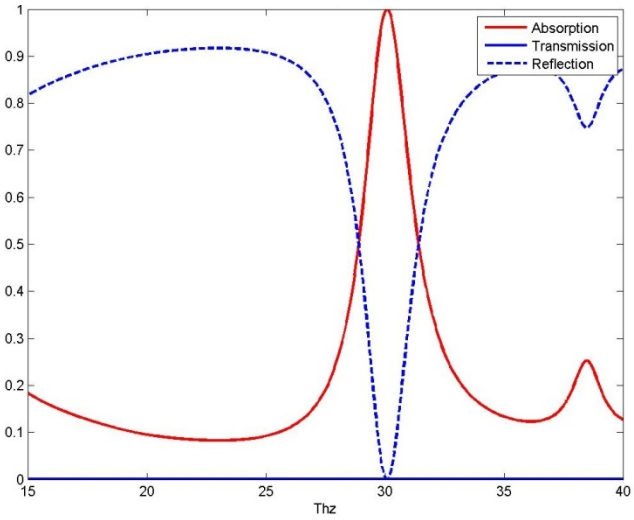

Figure 4.5 Power absorption, reflection and transmission of circular loop absorber: the red line, blue line and blue dashed line stand for power absorption, transmission and reflection, respectively.

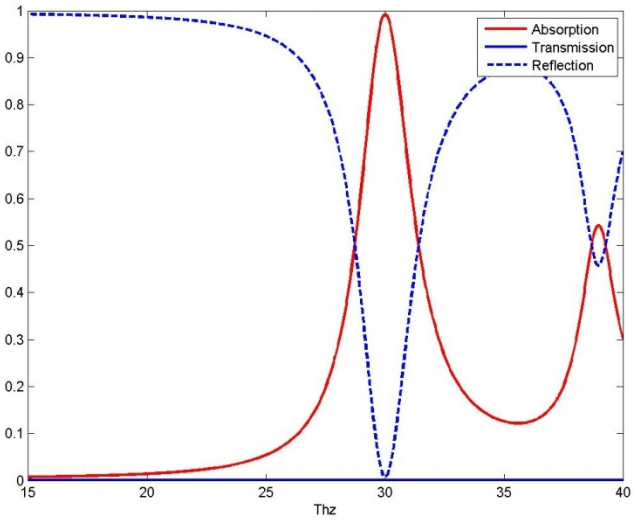

Figure 4.6 Power absorption, reflection and transmission of fishnet absorber: the red line, blue line and blue dashed line stand for power absorption, transmission and reflection, respectively.

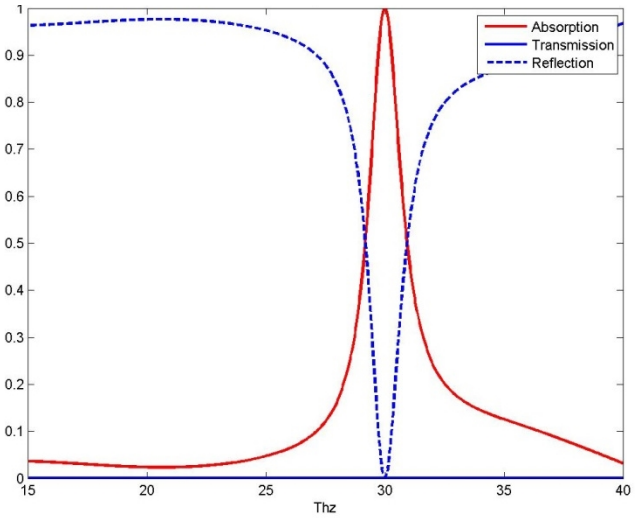

Figure 4.7 Power absorption, reflection and transmission circular patch absorber: the red line, blue line and blue dashed line stand for power absorption, transmission and reflection, respectively.

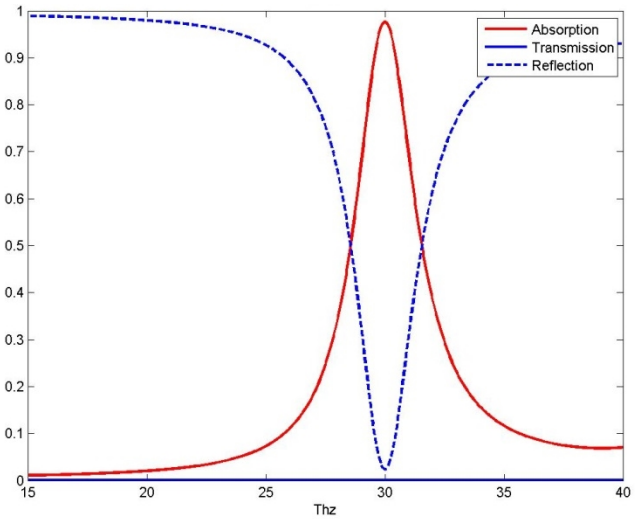

Figure 4.8 Power absorption, reflection and transmission of circular loop 2 absorber: the red line, blue line and blue dashed line stand for power absorption, transmission and reflection, respectively.

Figure 4.4 to Figure 4.8 show standard single cell designs, however there is an additional design that is important to present. A spiral absorber design is shown on Figure 4.9. Among the

many types of spirals, the type selected here is called the Fermat spiral which can be described through the equation

$$x = a\theta * \cos\theta; y = a\theta * \sin\theta \tag{4-14}$$

where a is a scaling factor for the spiral, and θ is the angle of the spiral line. To fit the spiral into a single cell and reserve space for two terminals, the equation is modified to

$$x = ra\theta * \cos(\frac{\theta}{2}); y = ra\theta * \sin(\frac{\theta}{2}). \tag{4-15}$$

where r is the radius of the spiral and a is still the scaling factor and theta is still the angle of the spiral line. For our design, parameters r = 0.1 and a = 2 were selected. A similar pattern was recommended in antenna design due to the broadband nature [44]. Different from absorbers with only one electrode material and 4-fold symmetry, this new type of absorber has 2-fold symmetry. Though it has a lower order of symmetry, the absorption spectrum is relatively broad as shown in Figure 4.10. A parametric comparison of different absorbers is shown in Table 4.2.

The pattern is divided into two legs of two different materials. The advantage of asymmetric geometry and materials is the asymmetric distribution of energy dissipation and corresponding temperature distribution that will be discussed in the next section.

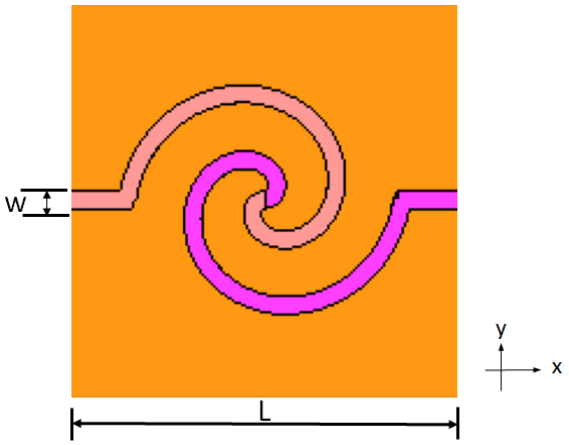

Figure 4.9 Top view of spiral design with dimensions L = 7.2 μm and w = 0.32 μm. Left arm is chromium and right arm is nickel.

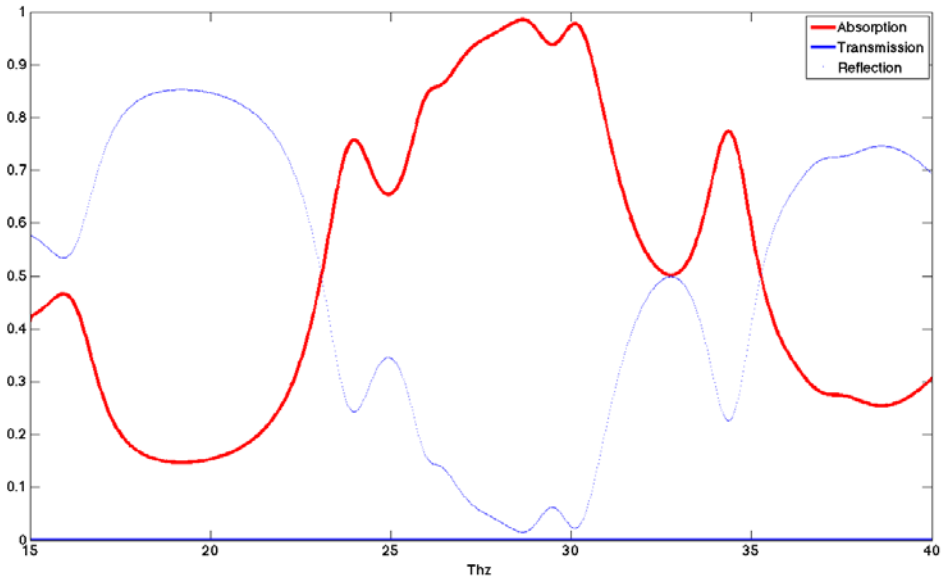

Figure 4.10 Power absorption, reflection and transmission of the spiral absorber: the red line, blue line and blue dashed line stand for power absorption, transmission and reflection, respectively.

Table 4.2. Q-factors of Different Designs

	f_c	Bandwidth (BW)	Q
Jerusalem cross	29.87	2.95	10.1
Circular loop	30.15	2.53	11.9
Fishnet	30.05	2.73	11.0
Circular patch	30.30	1.95	15.4
Circular loop 2	29.98	3.13	9.6
Spiral	28.65	12.23	2.3

4.1.3 *Energy Dissipation over Absorber*

Electromagnetic wave dissipation includes conductive loss, dielectric loss and magnetic loss. Since conductors have been formulated by the Drude model and magnetic loss is not considered due to non-magnetic assumption, dielectric loss is sufficient to describe electromagnetic dissipation over the structure. Some examples are demonstrated from Figure 4.11 to Figure 4.16.

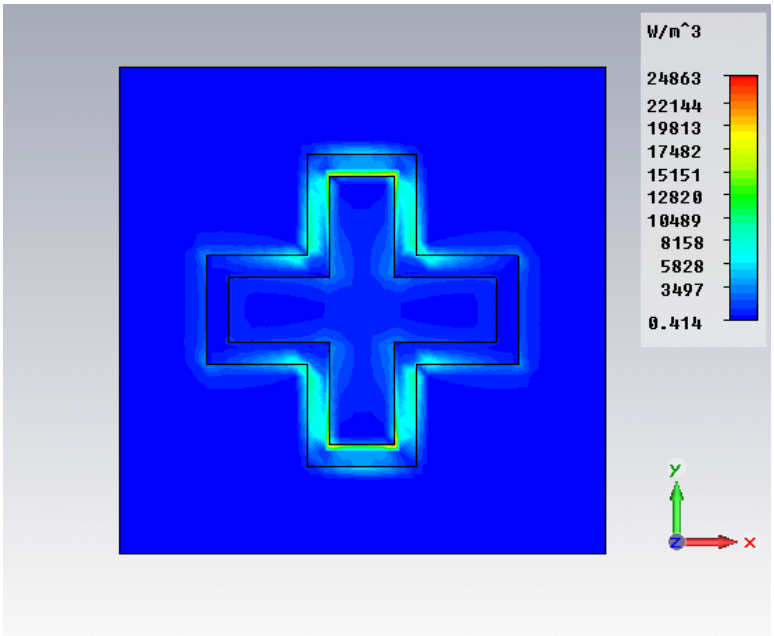

Figure 4.11 Electromagnetic energy dissipation over Jerusalem cross.

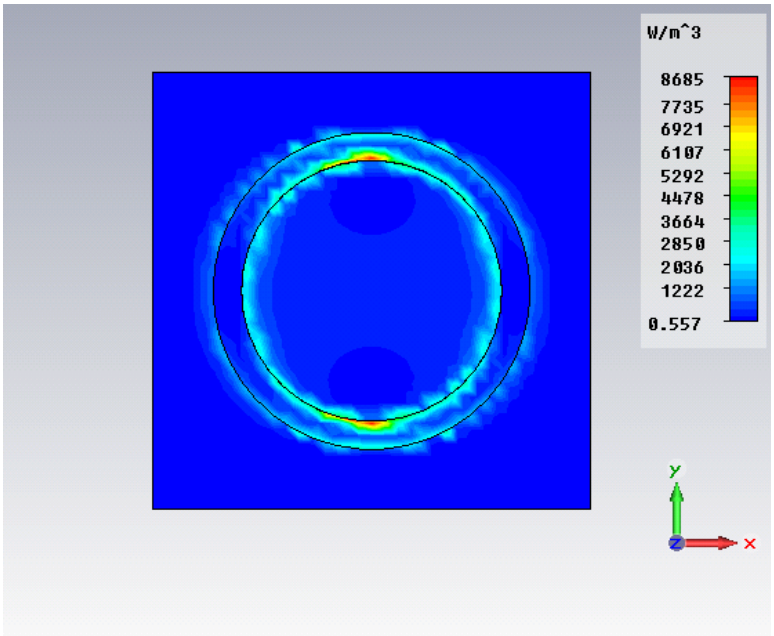

Figure 4.12 Electromagnetic energy dissipation over circular loop.

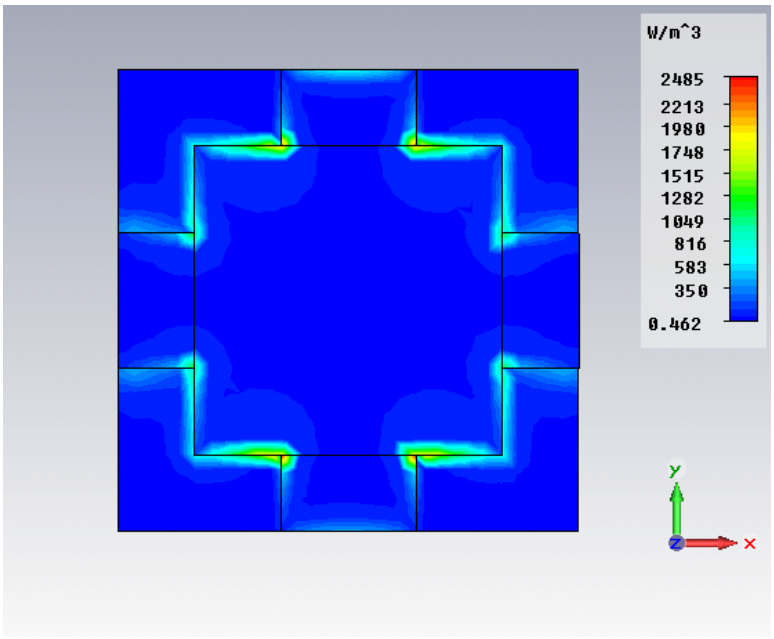

Figure 4.13 Electromagnetic energy dissipation over fishnet.

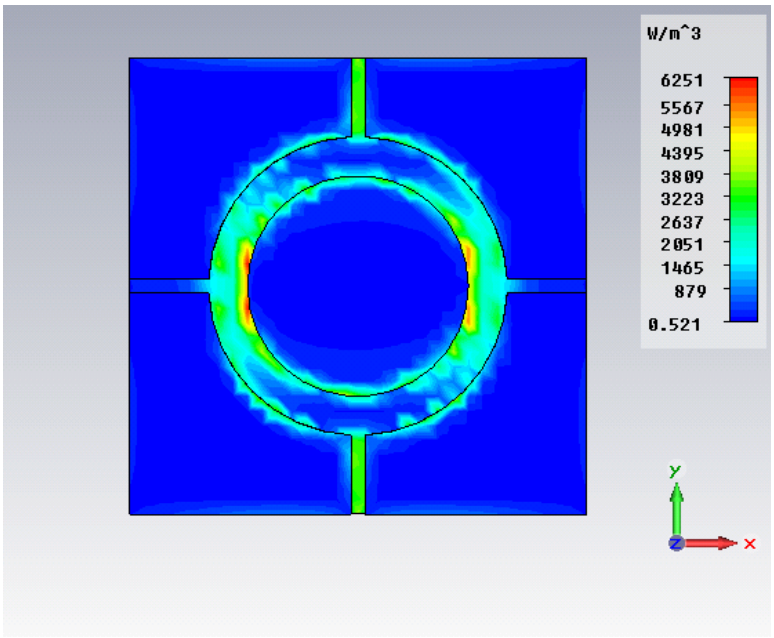

Figure 4.14 Electromagnetic energy dissipation over circular patch.

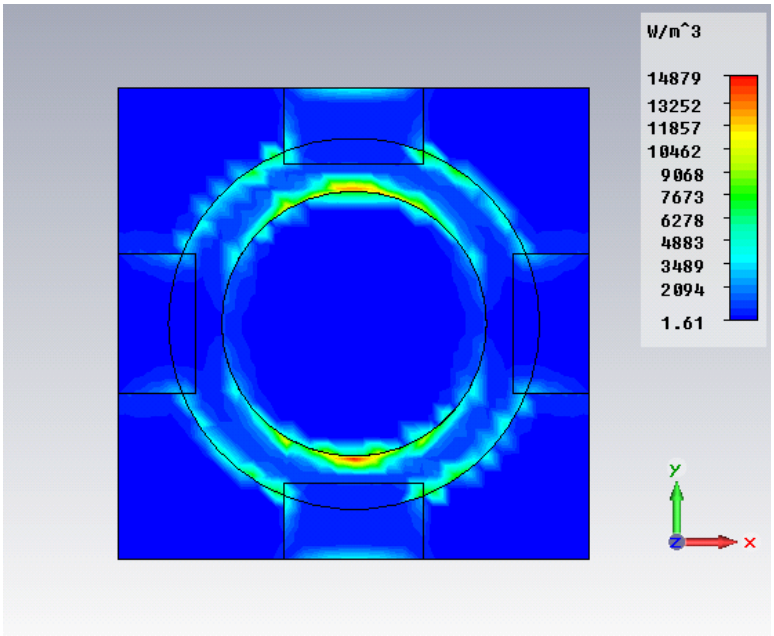

Figure 4.15 Electromagnetic energy dissipation over circular loop 2.

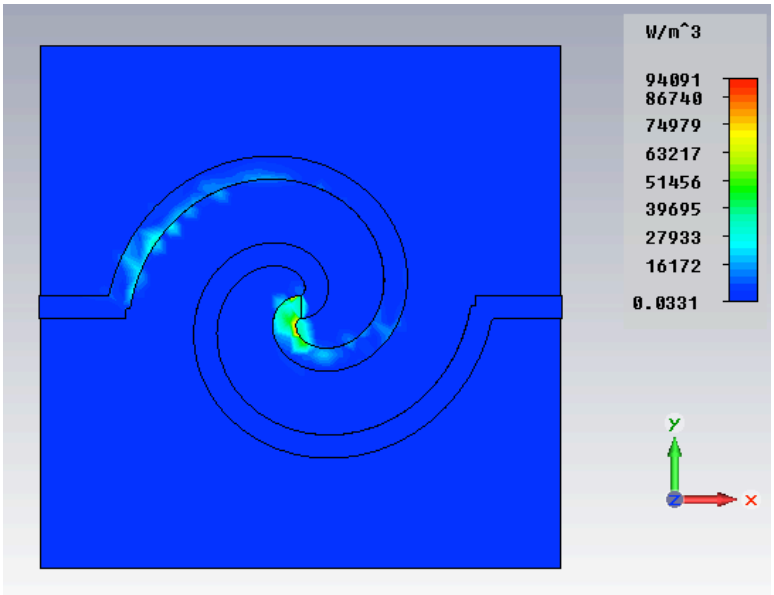

Figure 4.16 Electromagnetic energy dissipation over spiral.

Figure 4.16 shows that the spiral design has a clear asymmetric pattern appeared unique among all of the designs presented. The dissipation magnitude at the center is obviously greater than other parts away from the center. This is attributed to the geometric asymmetry and distinct material combination that was not used in traditional absorbers.

4.2 HEAT CONDUCTION AND TEMPERATURE FIELD

As shown in Figure 2.3, the device is designed for energy absorption in an ordinary daily environment, in which temperatures are close to 298 K (25 ℃). The power per unit area per unit wavelength is shown in Figure 2.4.

To estimate the radiation intensity at specific temperatures, integration is applied over the wavelength spectrum to calculate the power per unit area emitted by a distinct black body, which leads to the Stefan-Boltzmann law [45] shown in equation (4-16), where the Stefan-Boltzmann constant $\sigma_b = 5.670373 \times 10^{-8}$ $Js^{-1}m^{-2}K^{-4}$. The power per unit area of three different temperatures, 0 ℃, 27 ℃ and 100 ℃, is given in Table 4.3. According to the calculation, the reasonable range of intensity lies in the range between 100 and 1000 W/m^2.

$$I = \sigma_b T^4 \tag{4-16}$$

Though not specifically for our target application scenario, the longwave radiation which peaks around 10 μm is reported to have a 100 – 300 W/m^2 [46] intensity.

Table 4.3. Intensity versus Temperature

Temperature	273 K	298 K	373 K
Intensity (W/m^2)	315	447	1098

Since the device works continuously, the steady-state temperature distribution attracts more interests than the transient distribution. In the following calculation of thermoelectricity, the steady-state temperature distribution is applied in the calculation.

The heat diffusion equation shows

$$\nabla^2 T + \frac{\dot{q}}{k} = \frac{1}{\alpha}\frac{\partial T}{\partial t}, \tag{4-17}$$

where T is the temperature field, $\dot{q}$ is heat source, k is thermal conductivity and α is thermal diffusivity. Without the transient term, the temperature field is dominated by the heat source which is the energy dissipation of EM wave. To prompt temperature difference, maximization of energy absorption is therefore desired.

According to equation (2-3), a high temperature gradient is preferred for thermoelectricity generation. There are several directions to take in order to achieve this goal. From the EM designer's perspective, concentrated energy dissipation can increase the thermoelectricity generation.

Examples of energy dissipation are shown from Figure 4.13 to Figure 4.16. It is reasonable to predict the temperature field follows the pattern of energy dissipation since energy dissipation is the dominant term. Simulations of temperature field were conducted and the results are shown from Figure 4.17 to Figure 4.22.

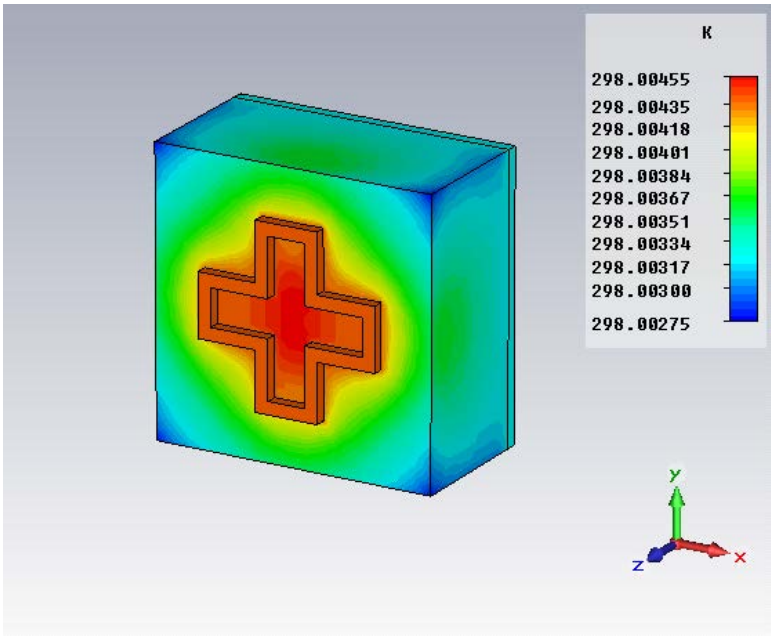

Figure 4.17 Temperature field over Jerusalem cross.

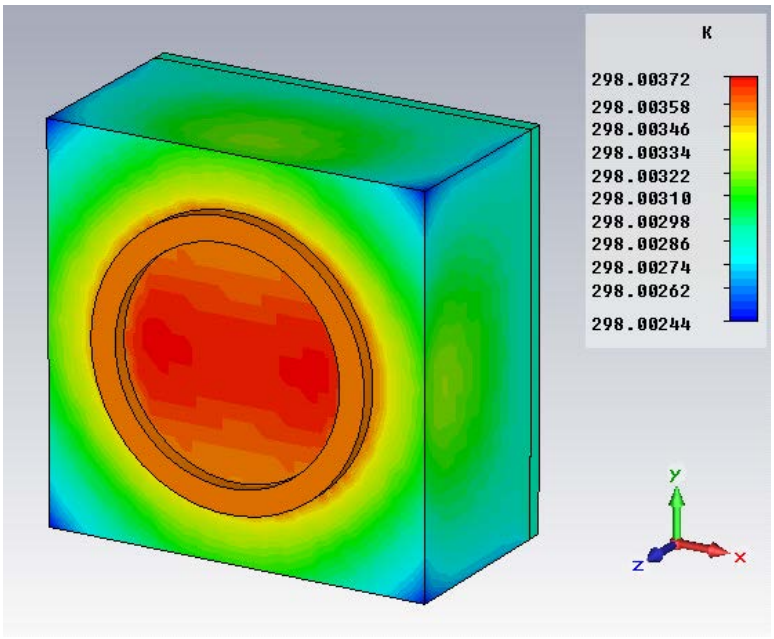

Figure 4.18 Temperature field over circular loop.

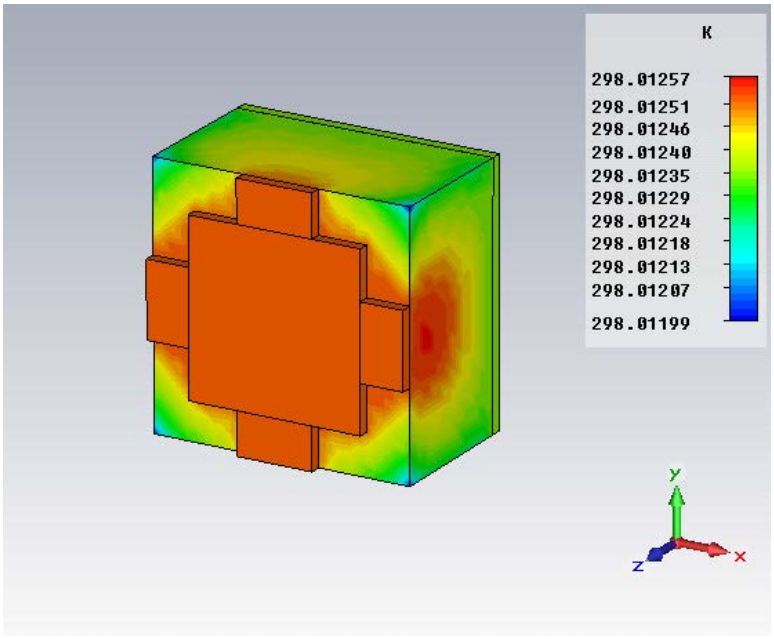

Figure 4.19 Temperature field over fishnet design.

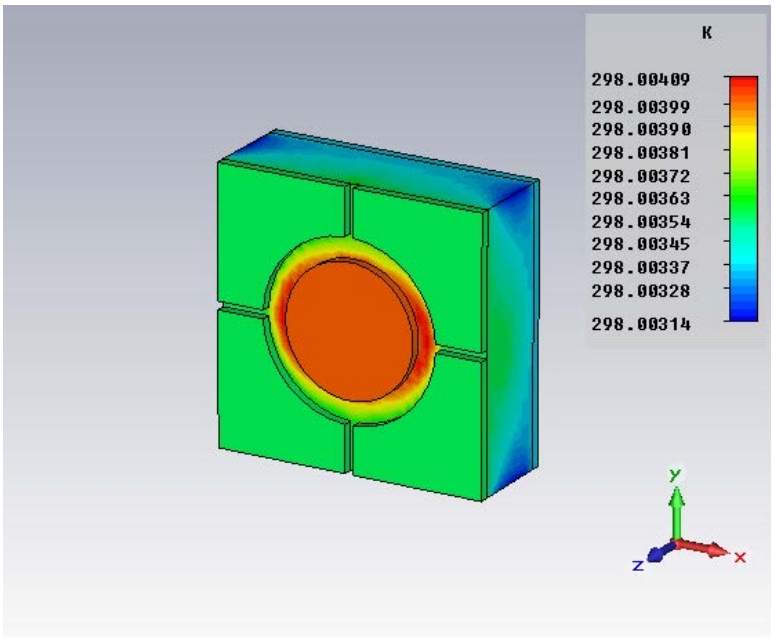

Figure 4.20 Temperature field over circular patch.

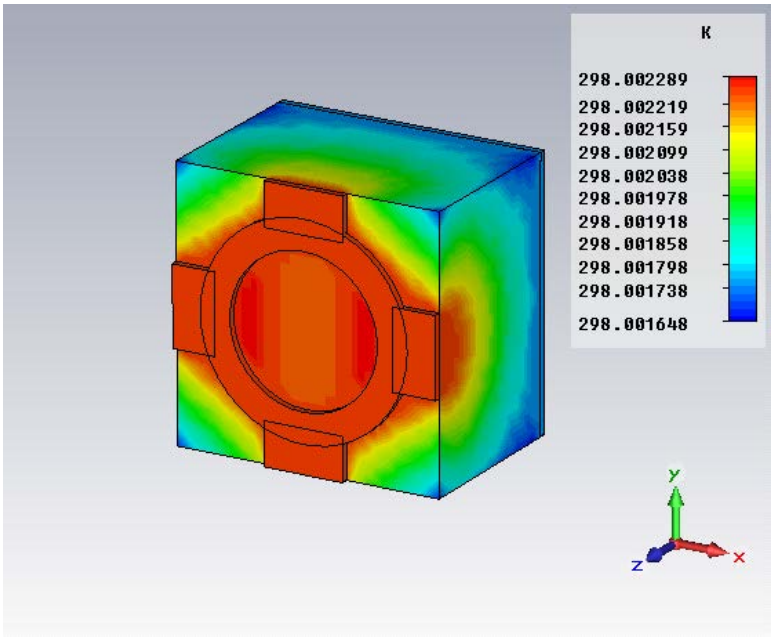

Figure 4.21 Temperature field over circular loop 2 design.

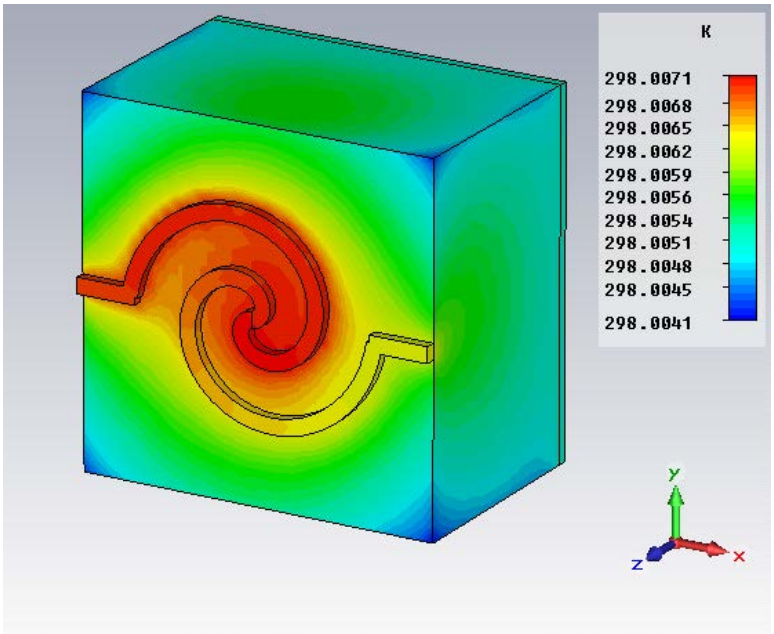

Figure 4.22 Temperature field over spiral design.

It is obvious from Figure 4.17 to Figure 4.22 that only the spiral design demonstrates asymmetric temperature difference in these figures. Besides asymmetric power dissipation pattern, the distinct top electrode combination enhances this temperature distribution, which can improve the output voltage.

4.3 THERMOELECTRIC VOLTAGE

Chromium and nickel are selected as top electrodes due to their material properties and manufacturing compatibility. These materials are common and have been applied in microfabrication for years. Given the temperature field, electric potential can be evaluated by relating electric field and temperature. Based on the Onsager reciprocity relation, a comprehensive equation to describe electric field in terms of electric current and temperature is given by

$$E_i = \sigma_{ik}^{-1} j_k + S_{ik} \frac{\partial T}{\partial x_k} \tag{4-18}$$

where σ_{ik}^{-1} is the tensor inverse of the conductivity tensor σ_{ik} and S_{ik} is Seebeck coefficient tensor [47]. Without connection to any external load, this is an open-circuit device. The contribution of electric current term shall not be considered. Since the material is homogeneous and isotropic, the open-circuit voltage can be evaluated as

$$V_{oc} = \int_{left}^{center} S_1 \frac{\partial T}{\partial x} dx + \int_{center}^{right} S_2 \frac{\partial T}{\partial x} dx. \tag{4-19}$$

where S_i is the Seebeck coefficient of each metal. The integration along x direction reflects the fact that single cell is connected along x direction. In FDTD, the structure is discretized by hexahedral meshes. Therefore, integration can be transformed into summation notation. The definition of left, center and right is depicted in Figure 4.23.

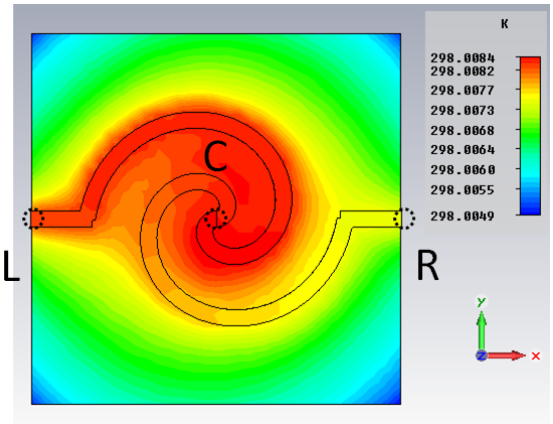

Figure 4.23 Temperature distribution over single spiral under normal incident 30 THz EM wave.

Based on the temperature field shown in Figure 4.22 and material parameters from appendix, the open-circuit voltage of spiral single cell is calculated to be -19.50 nV. This output of a single cell provides the fundamental for comparison and further improvement, for example, layout modification, intensity manipulation and material advancement.

4.4 Energy Harvesting Array Design

Normally, absorber materials include one metal for electrodes and one dielectric material for the substrate. Most of the design effort is in tailoring geometry or in optimizing the reflection and transmission. For broad-band absorption, multiple layers may be useful [48]. But that would increase complexity and manufacturing cost. Therefore broad-band using single layer is preferred.

Besides absorption optimization, temperature distribution is another key point for energy harvesting absorber. If the temperature distribution is symmetric, it will not be able to create

necessary temperature difference at the edges of design. Examples have been provided in section 4.1.3.

To introduce necessary temperature gradients, distinct metals are inserted into the design. Chromium and nickel fit bi-metal design requirements. Bi-metal design is common in thermoelectric devices but rarely seen in electromagnetic design. To accurately model the electrical properties, the Drude model is available for these two metals.

To create necessary temperature gradients, new absorbers are needed. The spiral design has been considered as one solution for broad-band design in antenna and metamaterial designs [49]. Another attractive feature is that it needs no multi-layer manufacturing. Metal deposition over single layer is sufficient.

With broad-band absorption, more radiation in the environment can be absorbed and more output can be generated. It is also noted that the temperature distribution of broad-band bi-metal design can be asymmetric. As shown in Figure 4.22, the temperature on the left end is higher than the temperature on the right end. This type of temperature field is favored because thermoelectric voltage can be generated across the two ends. Furthermore, a cascade connection of similar single cells can boost the output voltage.

The energy dissipation of an 11-by-11 array of the single cell spiral design is shown in Figure 4.24. With this distribution, the temperature field was simulated and is depicted in Figure 4.25. It is shown that the central part of the array has higher temperatures. This is a reasonable result since the heat is dissipated around the boundary and temperature field has lower values at the edges of complete array.

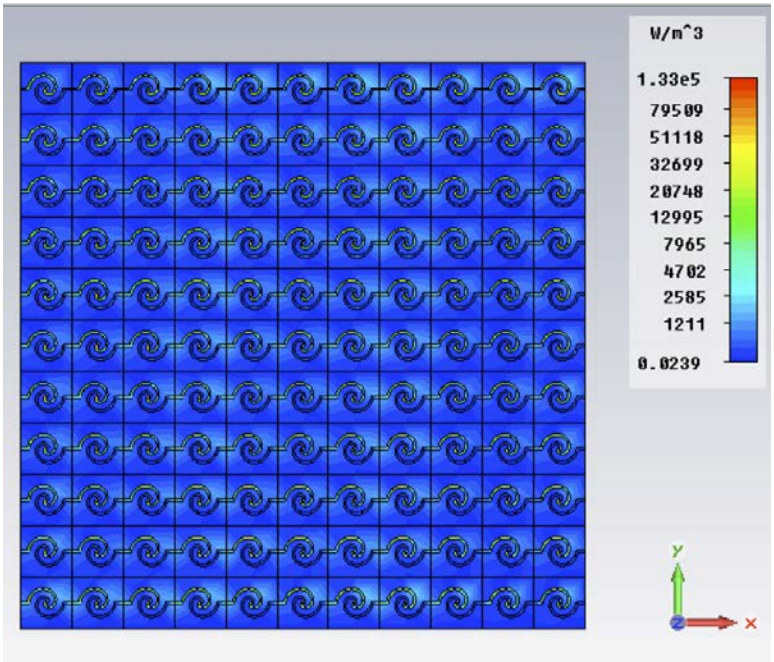

Figure 4.24 Energy dissipation distribution of an 11-by-11 spiral array.

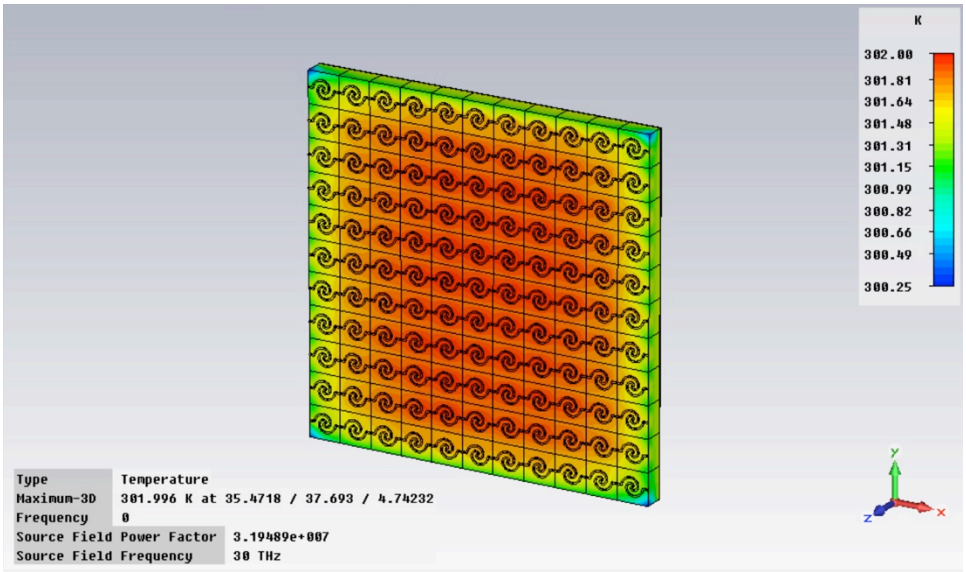

Figure 4.25 Temperature distribution of an 11-by-11 spiral array.

When the detailed temperature field is available, the complete voltage generation of each row can be evaluated. The voltage generated from each element is summed to evaluate the voltage of each row. Compared with the voltage generated from a single element, the voltage of each row is one order greater. Since this array is connected laterally, the voltage adds up in the lateral direction. If an electrical routing can be incorporated at the edges of the array, the total output voltage can increase by an order of magnitude.

To clarify the output characteristics of arrayed designs, several cases are evaluated and compared. The purpose is to verify whether the relation between voltage output and number of cells is linear or not. The following figures demonstrate the output voltages from a single cell, a 5-by-5 array and an 11-by-11 array. In these figures, V_{ri} represents the voltage from ith row. The first row is the row at the bottom of array. As mentioned above, this is a 2-fold symmetric design. Each cell is connected only in x direction.

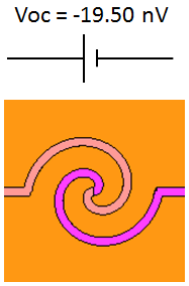

Figure 4.26 Voltage output of single spiral under normal incident at 30 THz.

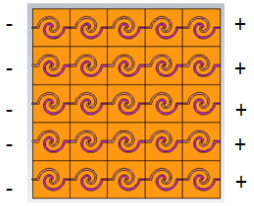

	Voc across each row (nV)
V_{r5}	121.6
V_{r4}	41.3
V_{r3}	41.3
V_{r2}	102.1
V_{r1}	104.4

Figure 4.27 Voltage output of a 5-by-5 spiral array under normal incident at 30 THz.

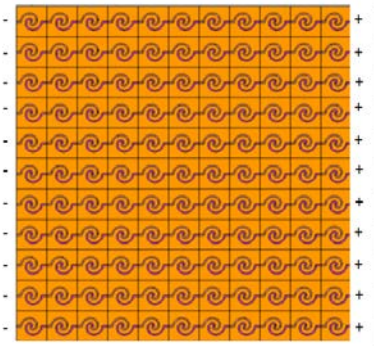

	Voc across each row (nV)
V_{r11}	121.6
V_{r10}	82.6
V_{r9}	184.7
V_{r8}	206.5
V_{r7}	165.2
V_{r6}	165.2
V_{r5}	206.5
V_{r4}	123.9
V_{r3}	206.5
V_{r2}	154.3
V_{r1}	228.3

Figure 4.28 Voltage output of an 11-by-11 spiral under normal incident at 30 THz.

Since arrays of different sizes have different numbers of rows, it is incomplete to simply look at the voltage output of each row. In addition, the sign of voltage depends on the definition

of electrical polarity. Hence, comparison of absolute values is recommended. Assuming the output of each row can be eventually combined, it is meaningful to count the summation of row outputs. The average of row outputs within one array was calculated and is shown in Figure 4.29. The average of row outputs is defined as $V_{ave}=\frac{1}{n}\sum_{i}^{n}V_{ri}$, where *n* is the number of rows or dimension of array.

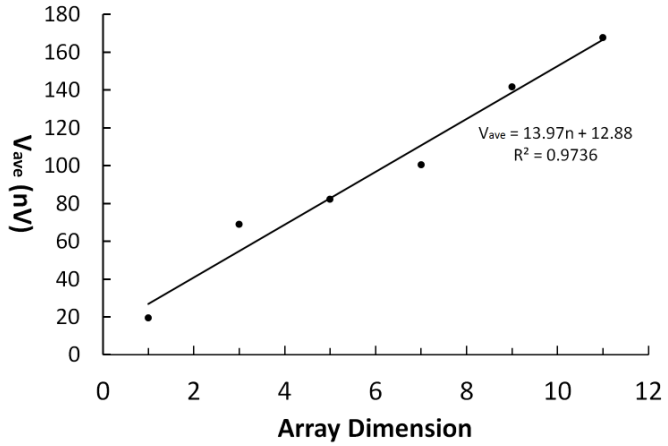

Figure 4.29 Averaged voltage output versus array dimension.

As shown in Figure 4.29, when the dimension of the array increases, the output voltage increases as well. A relation between the averaged output voltage and array dimension is estimated by $V_{ave}/V_{SingleCell}=R\times n$, where $V_{SingleCell}$ is the output of a single cell in Figure 4.26 and *R* is a variable to estimate the imperfection of the arrayed structure. For example, 5-by-5 and 11-by-11 arrays show *R* values as 84% and 78%, respectively. A linear regression result shows $V_{ave}=13.97\times n+12.88$ and a 0.9736 coefficient of determination. This discovery implies the array output increases linearly with slight imperfection. Besides the boundary effect, the imperfection comes from the interaction between each cell, especially when the cell is asymmetric. This imperfection evaluation provides a reference when scalability is required to meet various voltage output requirements.

4.5 Energy Harvesting Cell Design Layout Improvement

Under the original scheme, concatenating different rows to boost voltage output could be difficult because of the identical electrical polarity between single cells. Additional routing or via structures are needed to achieve this goal. However, these additional structures might affect the

energy dissipation pattern and therefore the temperature field. One electrical layout is proposed to overcome this issue by reversing the electrode materials every other row. This idea is shown below by the schematic in Figure 4.30.

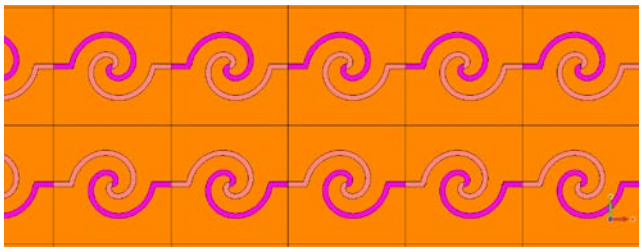

Figure 4.30 Proposed electrical rout to switch electric polarity of every other row.

The S-parameters also suggest this change of electrode material does not alter the trend of transmission, reflection and therefore the absorption spectrum. The S-parameters were simulated using an FDTD simulation and the proposed design shown in Figure 4.30. The simulated S-parameters are shown along with S-parameters from the original design depicted in Figure 4.31.

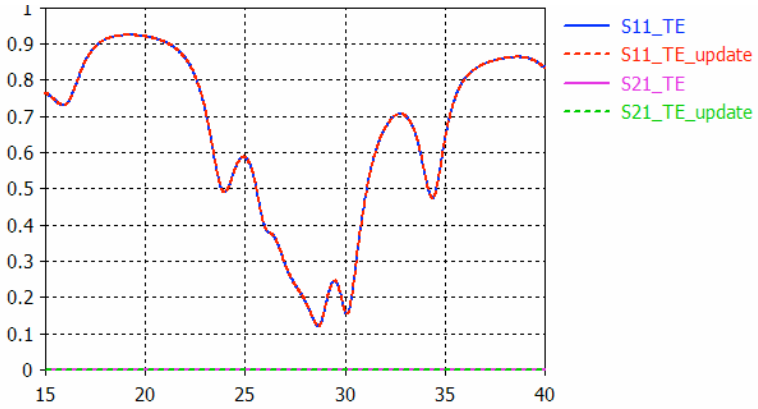

Figure 4.31 S-parameter comparison of original and proposed (updated) designs.

Given that the absorption spectrum should not change with the mentioned change in the design layout, an EM-thermal evaluation was performed. The evaluation for a revised 11-by-11 array is shown in Figure 4.32. The results suggest that the electrical polarity switches every other row due to the switching of electrodes.

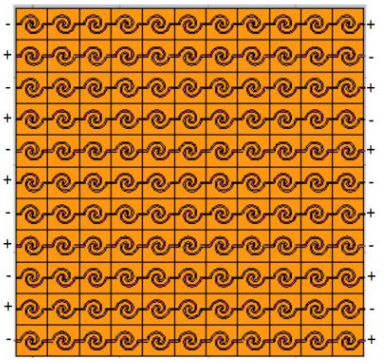

	Voc across each row (nV)
V_{r11}	80.3
V_{r10}	143.3
V_{r9}	165.2
V_{r8}	165.2
V_{r7}	123.9
V_{r6}	123.9
V_{r5}	123.9
V_{r4}	82.6
V_{r3}	123.9
V_{r2}	143.4
V_{r1}	104.4

Figure 4.32 Voltage output of revised 11-by-11 spiral array under normal incident 30 THz EM wave.

Though the *R* value of this proposed design drops to 58%, the series connection can be made possible without additional routing. In other words, the output can be enhanced by one order by serially connecting adjacent rows near the boundary.

Chapter 5. EXTERNAL PASSIVE INTENSITY BOOSTER

The temperature gradient decides the output of EMTE cells. In addition to the intrinsic design change of shape and materials, an extrinsic solution is proposed to change the intensity distribution of incident wave.

An external device is applied over the EMTE device. Periodic slits or gratings can scatter the incident wave into diffracted patterns. Assuming one plane wave is passing through such structure, the relation between incident angle, diffraction angle and periodicity can be related at optical frequencies [50]. Figure 5.1 shows such a structure for 30 THz.

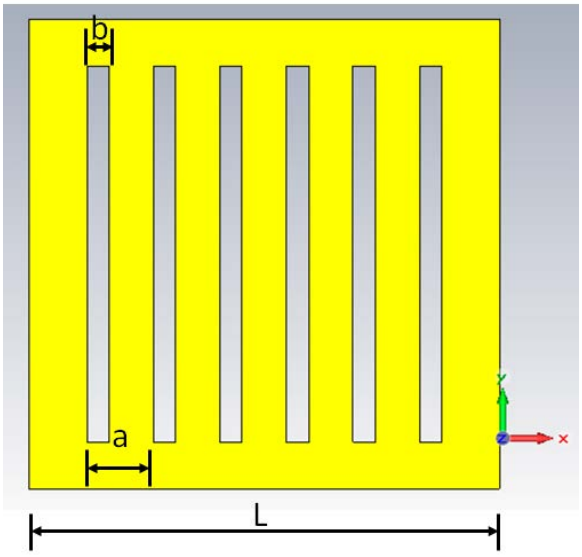

Figure 5.1 One example of gratings: L = 100 μm, a = 14.14 μm and b = 4.71 μm.

The electric field amplitude can be used to determin the points of interest in a 3D domain. The Computer Simulation Technology (CST) default amplitude of input electric field is 1 V/m, pointing in the y direction. If there are some points with higher values, the intensity of those points is considered boosted. When a plane wave encounters the periodic silts in Figure 5.1, the electric field is distributed and is demonstrated in Figure 5.2, where some points show the magnitude greater than 1 V/m. There are several interesting points that possess a higher value of E_y field than the default value. If EMTE cells are placed at these points, a higher temperature gradient would be expected.

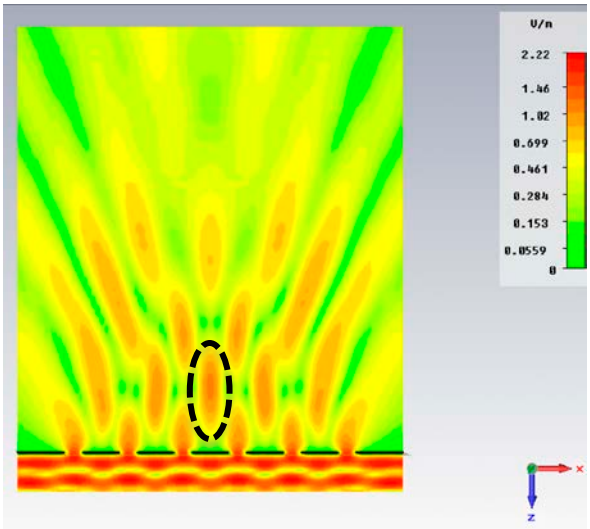

Figure 5.2 The E_y amplitude distribution of a s-polarization wave at 30 THz passing through a structure in Figure 5.1. The observation xz plane is cut at the center of the simulation domain.

To verify whether locally boosted intensity improves the temperature gradient and thus voltage output, thermoelectric simulations were conducted. First, the EM wave disturbance due to the single EMTE cell was evaluated. Second, the energy dissipation pattern, temperature distribution and output of this single cell was evaluated.

Without a EMTE cell, the plane wave diffusion is demonstrated in Figure 5.3 (a). Due to the insertion of the EMTE cell, clear disturbance can be seen in Figure 5.3 (b). According to the wave pattern shown in Figure 5.2, the single cell is chosen to be placed at the directional center after the EMTE cell.

(a) without EMTE

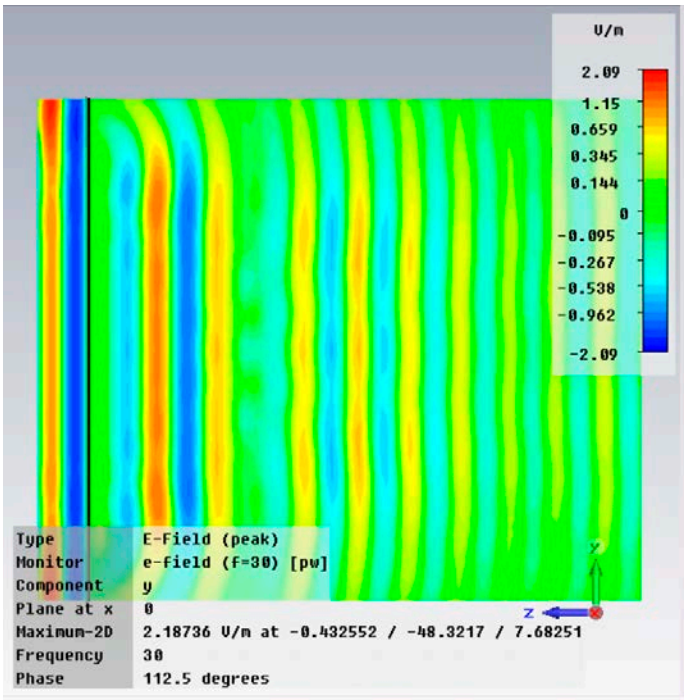

(b) with EMTE

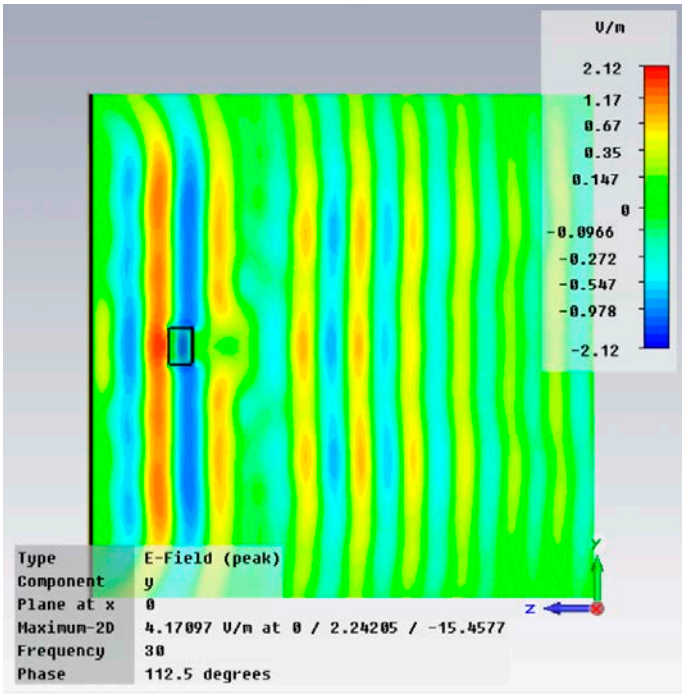

Figure 5.3 E_y distribution of a s-polarization wave at 30 THz. The observation yz plane is cut at the center of simulation domain: (a) without EMTE; (b) with EMTE.

The Figure 5.3 shows that the EMTE disturbs and absorbs the incoming wave. The corresponding energy dissipation pattern over the EMTE is depicted in Figure 5.4. Comparing Figure 5.4 with Figure 4.16, dispersed energy is discovered in Figure 5.4.

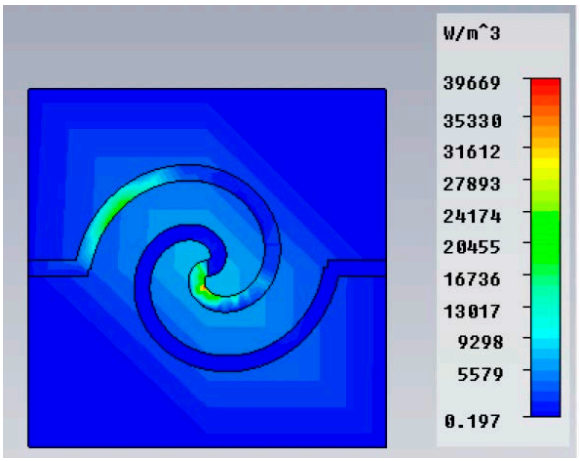

Figure 5.4 Energy dissipation pattern of a single EMTE cell from a 30 THz EM wave passing through a diffraction grating in Figure 5.1.

The corresponding temperature field from the simulation using the diffraction grating is shown in Figure 5.5. The temperature field turns out to be uniform over the top electrode and contributes nearly zero voltage output.

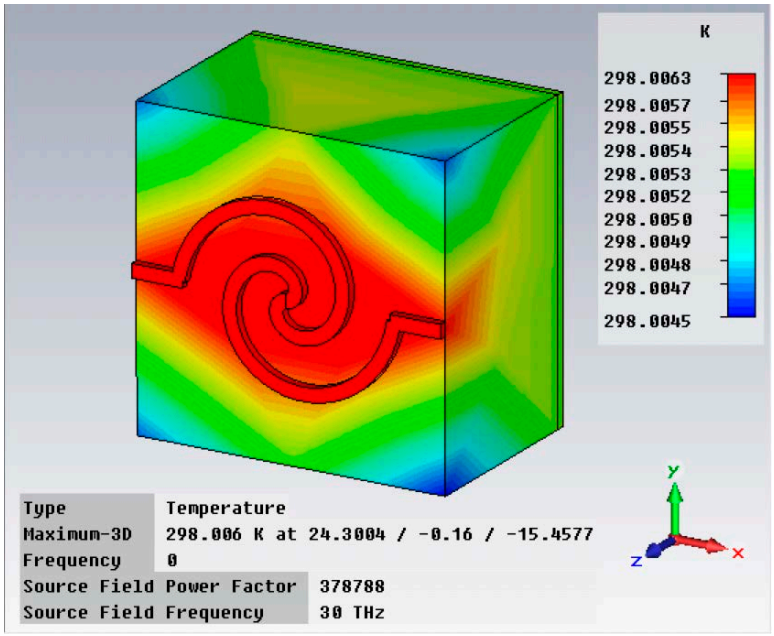

Figure 5.5 Temperature field of single cell after 1D grating device.

Since the first intensity booster doesn't improve voltage output, a second intensity booster is proposed as Figure 5.6. This is a 2D grating supported by SU8. Besides better intensity enhancement, this 2D grating demonstartes more concentrative intensity dispersion than the 1D grating. To visualize the intensity enhancement, the intensity (magnitude of the Poynting vector) were ploted over an obervation plane parallel to this 2D grating. This is shown in Figure 5.7.

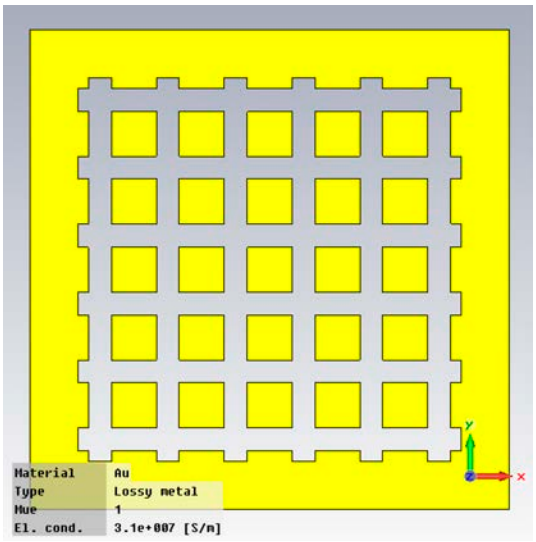

Figure 5.6 The design of 2D grating for a 30 THz incident EM wave (Front View).

As mentioned, the default value of the electric field in the simulation domain is 1 V/m. Since the impedance of air is around 376 Ω, the square of electric field divided by this impedance results in input intensity around 0.00264 VA/m^2. Besides comparing electric field magnitude, comparing intensity is another way to show intensity boost.

There are several points showing possible intensity enhancement in Figure 5.7. The center of this obervation plane seems to have greatest intensity enhancement. To see the exact values at interesting points, an observation line is drawn over the observation plane as shown in Figure 5.8. The intensity profile along this line is presented in Figure 5.9. The central peak on the obervation plane shows 36% intensity enhancement. It is also interesting to see the intensity profile is different from the normal sinc function profile in an optical grating [50].

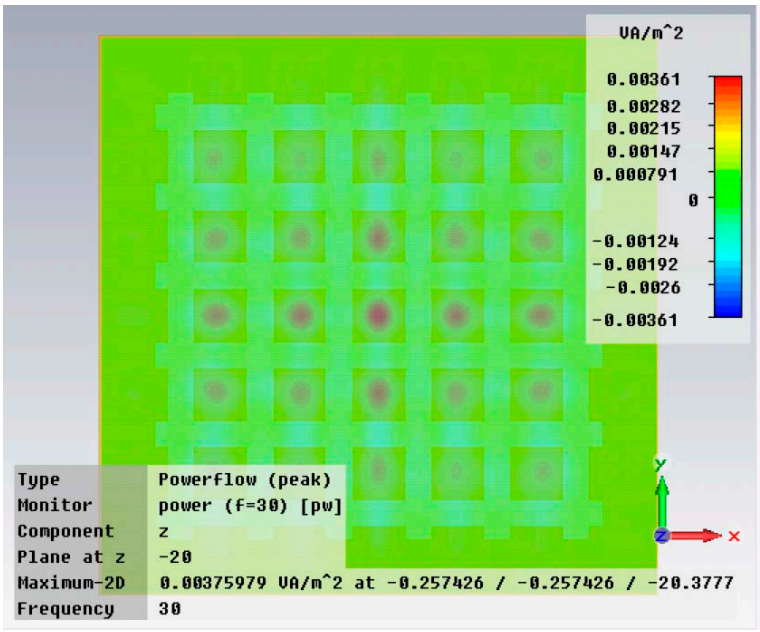

Figure 5.7 P_z magnitude on xy plane 2.0 wavelengths away from 2D grating at 30 THz.

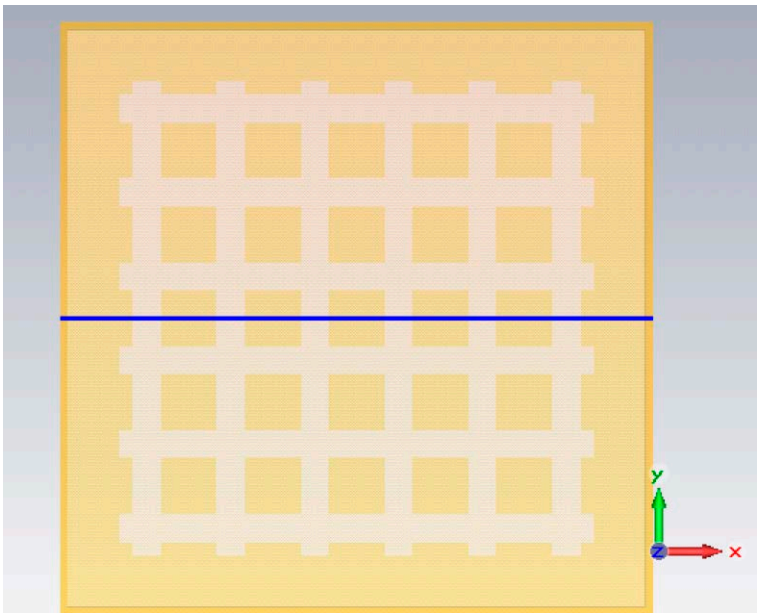

Figure 5.8 A front view of the 2D grating with an observation line drawn.

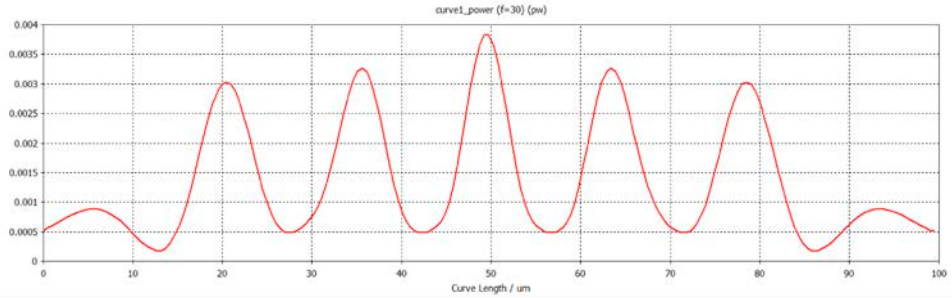

Figure 5.9 The intensity profile along the specified observation line shown in Figure 5.8.

When the center of an EMTE cell is aligned with the high intensity peak point of the EM wave, greater thermoelectric output is expected. The alignment of a EMTE cell is shown in Figure 5.10. The single cell is also tested with the 2D diffraction grating and the correponding temperature distribution is given in Figure 5.11.

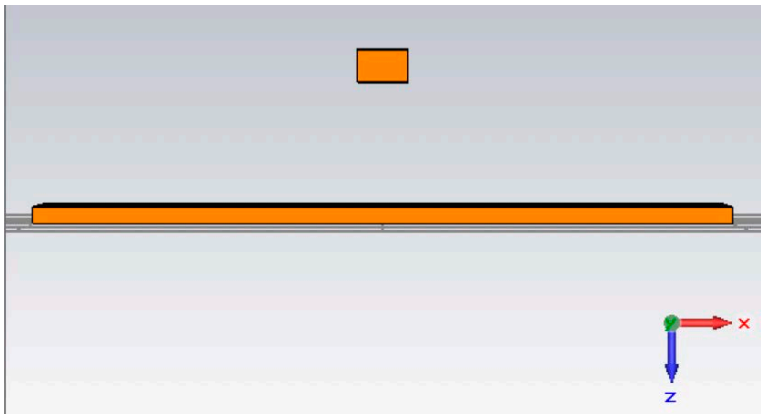

Figure 5.10 The alignment of EMTE single cell and 2D grating intensity booster.

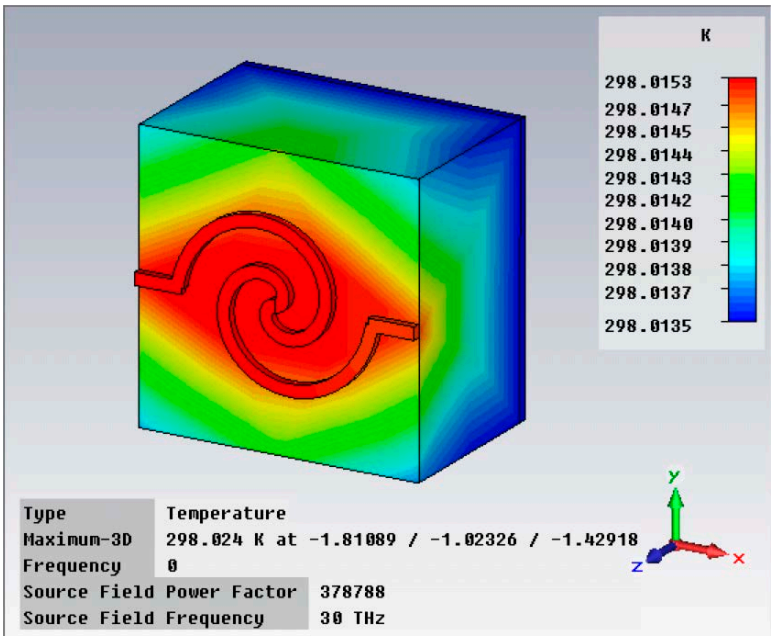

Figure 5.11 Temperature field distribution of a single spiral cell after a 30 THz wave passes through a 2D diffraction pattern.

Even though the intensity is enhanced, a preferred temperature gradient is not created over spiral structure. Looking at the Poynting vector of the 2D grating in Figure 5.12, it is obvious that the incident wave becomes a synthesis of various oblique incident waves. As reported in [51], the absorption of oblique incident wave is relatively low. On the other hand, the incident wave is modulated by the 2D grating device. The modulated wave doesn't necessarily create the same energy dissipation pattern modeled in plane wave incident case.

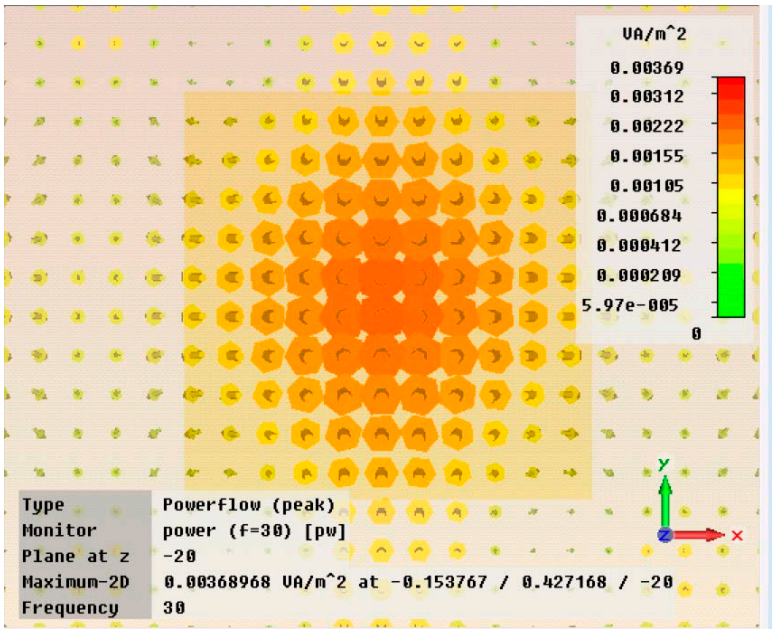

Figure 5.12 Poynting vectors upon the EMTE single cell after a 30 THz wave is passing through a 2D diffraction grating as shown in Figure 5.10.

Reviewing Figure 5.9, the distance between the central intensity peak and the first dip on the right side is about 7 μm which is close to the domain size of EMTE cell (7.2 μm). When the EMTE is moved to the middle of this central peak and first right dip, a temperature difference is enforced over EMTE single cell. The idea is demonstrated and verified in Figure 5.13.

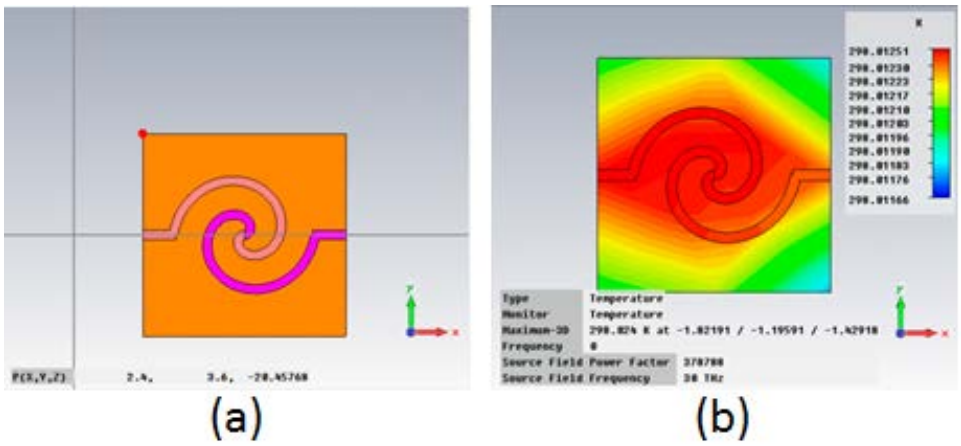

Figure 5.13 The EMTE shifts by 6 μm to positive x direction. (a) The plot shows the top view; (b) the plot shows the temperature distribution.

The voltage output of this EMTE single cell is found to be 21.8 nV as shown in Figure 5.14. This is different from original value -19.5 nV without a diffraction grating. In addition to the change of sign, the magnitude of voltage output is improved by 11.79%. After reviewing the

temperature distribution, it is found that the positive output mainly comes from the temperature gradient on the left arm (10^{-3} K difference from left terminal to center) while the right arm contributes nearly no temperature gradient. This discovery shows the 2D grating improves the output mainly through heat conduction.

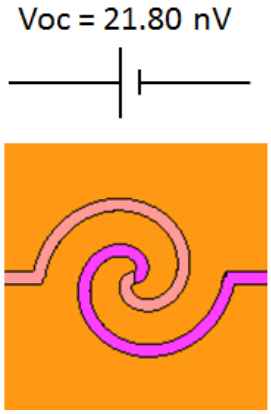

Figure 5.14 Voltage output of single EMTE spiral after a 30 THz wave is passed through a 2D diffraction grating as shown in Figure 5.10.

Chapter 6. CONCLUSION

An EMTE device is proposed to provide continuous energy supply and portable flexibility. The 30 THz operation frequency of the EMTE device can find great potential in some environments where the energy source is limited, for example cities at high latitudes or satellite operation behind the shadow of the earth. By integrating TE materials into an EM wave energy absorber, continuous conversion of EM waves into DC voltage output is possible. In the proposed bi-metal spiral design, a 19.5 nV output is available within a 7.2 μm square area of a single cell.

As shown in different cell array arrangements, the voltage output per row may be different. This phenomenon could be from the asymmetry of the single cell. Therefore, the expectation of symmetric or uniform voltage output per row is hardly satisfied in the spiral design case.

An EMTE array increases the output linearly with respect to the number of concatenated single cells. This linearity is useful in the evaluation of required cells for specific applications. One such example that could benefit from the proposed design being scaled is the sub-300 mV RF receivers [52].

To further concatenate the voltage output per row, it is beneficial if each row is connected. Due to the limit of electrical polarity, however, additional routing is required to achieve this purpose. A suggested solution is switching the electrode material appropriately, changing the electrical polarity but not changing the absorption spectrum. Under such a scheme, additional routing or via structure can be avoided in serial connection. This scheme provides a practical and economical solution for bi-material design.

Besides intrinsic improvement for a single cell, extrinsic modification is sought as well. Additional devices are incorporated to disturb the energy distribution over the EMTE single cell. A passive diffraction grating provides 11.9% improvement over single cell by concentrating the incident EM wave. However, the incident wave pattern triggers a response over the EMTE single cell that deviates from our expectation. In addition, the incident wave turns out to heat up not only the top electrodes but also the supporting substrate. The substrate is thus a thermal conducting channel which disperses energy into unflavored directions.

Finally, unlike a traditional TE generator attached to a fixed heater or pipeline, and unlike photovoltaic cells for solar energy production, this EMTE device targets 30 THz radiation from

environmental heat sources, such as the human body or electronic appliances. It is free to move without much restriction. To enhance the output of such a design, we plan to incorporate other materials and structures that prompt more temperature gradients in future work.

Chapter 7. FUTURE WORK

Traditional energy absorbers demonstrate high absorption and a broadband spectrum. These attractive features have been embedded in the proposed spiral bi-metal design. In addition, the proposed design further provides a favored temperature gradient which allows more voltage output per singe cell.

Another proposal of switching top electrode materials every other row keeps the original EM wave features and provides an easy way to sum voltage output of each row. This combination could provide a one-order improvement for voltage output and avoids complicated electrical routing.

It is expected that continuous voltage improvement will alleviate the requirement of device size and enhance the portability. Some directions are promising to achieve this goal. They include the application of advanced materials, especially phonon glass electron crystal [53]. Other directions include the delicate design of a single cell and the implementation of external devices to control energy distribution.

7.1 MATERIAL RESEARCH

It is known that TE materials have a figure-of-merit zT, which is a function of temperature. In other words, to achieve a best figure-of-merit value, distinct TE materials are required in different temperatures. Matching a pair of materials can lead to a more delicate discussion whether maximum output or maximum efficiency is the requirement [22]. Intuitively, higher temperature difference can be achieved by lowering thermal conductivity. However, a lower thermal conductivity normally leads to a lower electrical conductivity. In other words, the coupling between thermal conductivity, electrical conductivity and the Seebeck coefficient is subtle [54].

Phonon glass electron crystal material have been investigated to decouple these quantities [53]. This type of material has low phonon thermal conductivity while keeping the electron conductivity high. The localization of thermal energy is improved with sustained electron current conduction. However, there are rare studies investigating the EM properties of such materials which are as important as the TE figure-of-merits.

Another issue for the materials selection in an absorber design is the manufacturing compatibility. Due to the target frequency being around 30 THz, micro-fabrication is inevitable. New material growth processes must be developed and be compatible with current micro-fabrication processes [55].

7.2 Single Cell Design Topology

The shape of a single cell is considered as intrinsic as the materials making up the single cell. Spiral design leads to the realization of high energy concentration over a broad-band spectrum which leads to better voltage output. There are other designs which show broad-band feature as well [8]. Besides, different types of lattices could be incorporated to tailor the bandwidth of absorption [56].

7.3 Development of External Devices

To boost output voltage, there are passive and active solutions to manipulate the energy distribution. Passive gratings have demonstrated the ability to enhance incident intensity. However, they do not necessarily follow optics predictions (Chapter 5) and therefore require careful verification.

Gradient-index (GRIN) lenses are able to provide a light focusing function [57]. To add more flexibility, electrically active materials can be implemented as composition materials of a GRIN lens. The functionality of active materials has been demonstrated in our previous research of active metamaterials [38]. The tuning flexibility endows unlimited operation modes into single device. With a 10-by-10 planar gradient device shown in Figure 7.1, 1D tuning can be achieved by controlling electrical signals over top and bottom electrodes, respectively.

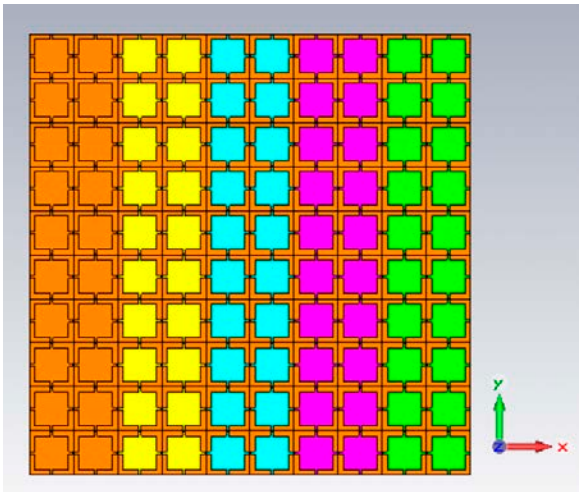

Figure 7.1 Top view of a case of planar gradient (10-by-10) device. The top and bottom electrodes are hidden for visualizing tuning conditions. Each color corresponds to the dielectric constant in Table 7.1.

Table 7.1. Listing of The Material Properties in Figure 7.1.

	Relative Permittivity: ε_r	Conductivity (S/m)
Au (normal)	N.A.	3.1×10^7
Dielectric – brown	2.5000	N.A.
Dielectric – yellow	2.4375	N.A.
Dielectric – blue	2.3750	N.A.
Dielectric – purple	2.3125	N.A.
Dielectric – green	2.2500	N.A.

In Figure 7.2, a 600 μm wide square waveguide is located at the bottom of the simulation domain. It is emitting electromagnetic waves into the negative z direction. Since the waveguide is aligned with the planar gradient, this is a normal incident condition. As the wave passes through the planar gradient, the device shifts the wave to the left.

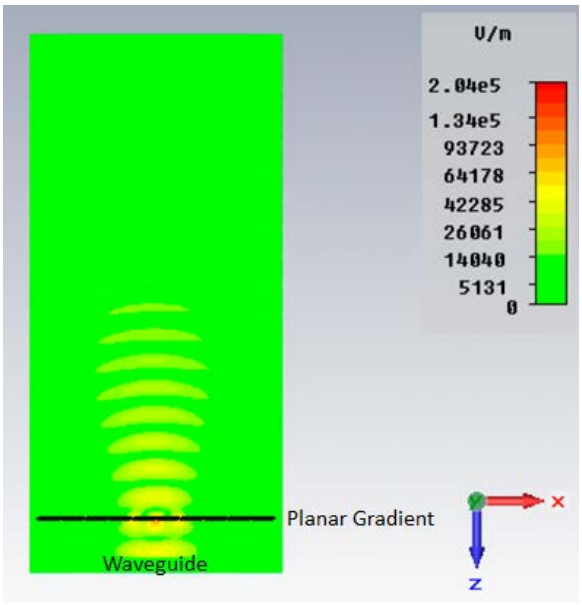

Figure 7.2 E-field (absolute value) over a planar gradient device at 0.91 THz normal incidence.

Besides this case, there are innumerous tuning patterns that could potentially create exotic phenomena. However, more verification of the gradient index profile is needed to optimize the performance of similar devices. In addition, the control algorithm and electrical routing need to be addressed in the near future.

7.4 FABRICATION PROCESS

There are two directions for the fabrication of the EMTE energy harvesting device. The first one is a customized fabrication processes developed by ourselves; the second one is a combination of foundry processes and post-processes. The CMOS foundry services have been developed for years and they can be good options. Some fabrication options were proposed in Figure 7.3. Considering the cost and complexity of development, only two options are discussed in this section. They are based on nano-imprint and CMOS process, respectively.

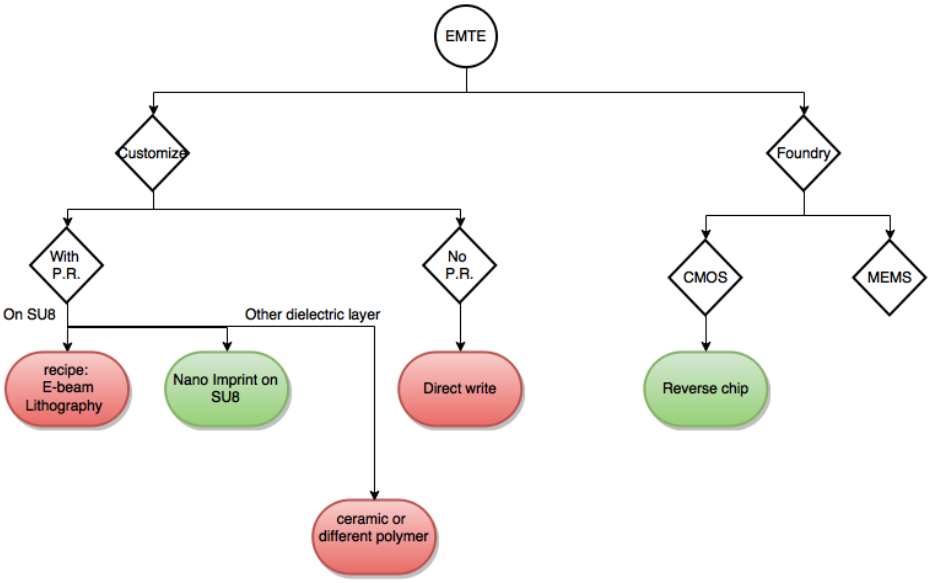

Figure 7.3 Potential fabrication processes.

E-beam lithography has shown capability to fabricate an array of 20 nm-wide lines with 40-nm pitch [58]. The dimensions are much smaller the EMTE feature sizes.

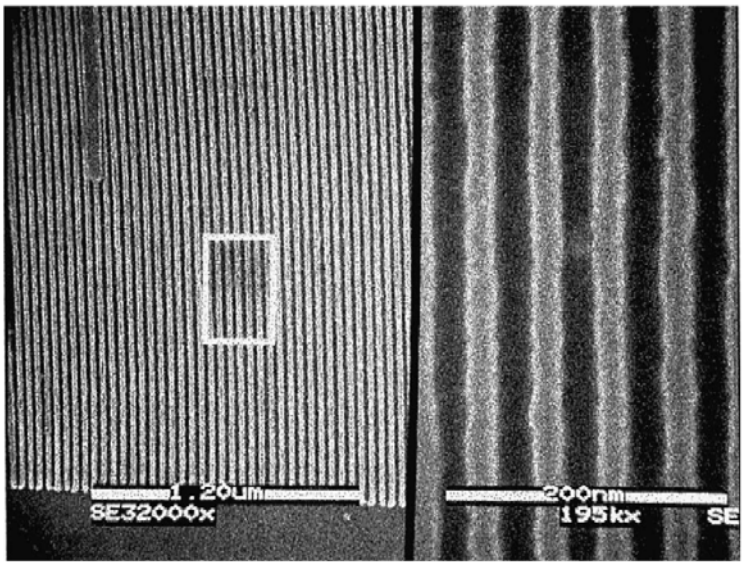

Figure 7.4 SEM image of a 20-nm line array after nickel lift-off and reactive ion etching (RIE). It was developed in pure IPA assisted by ultrasound agitation [58].

An annular structures was also fabricated and reported in Washington Nanofabrication Facility (WNF) [59]. Figure 7.5 demonstrates a fully etched coupler for TM mode. The structural dimensions are estimated based on the paper data and attached as Table 7.2.

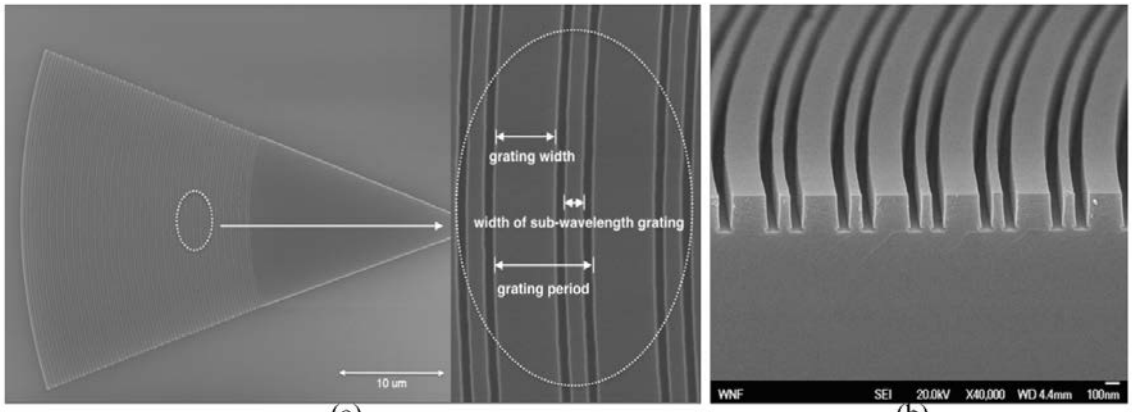

Figure 7.5 SEM of focusing sub-wavelength gratin coupler. (a) top view; (b) sidewall view [59].

Table 7.2. Structural Dimensions of Fully-etched Sub-wavelength Grating

Grating width	575 nm
Sub-wavelength grating width	140 nm
Grating period	960 nm
gap	123 nm

It is noted that the annular structure is similar to the spiral. The processes could be applied to fabricate a spiral structure as a mold. Then, the mold can be applied in nano-imprint process to replace repeated e-beam lithography.

A mold creation process is outlined in Figure 7.6. The corresponding e-beam lithography recipe and dry etching recipe can be referred in Table 7.3 and Table 7.4, respectively [59].

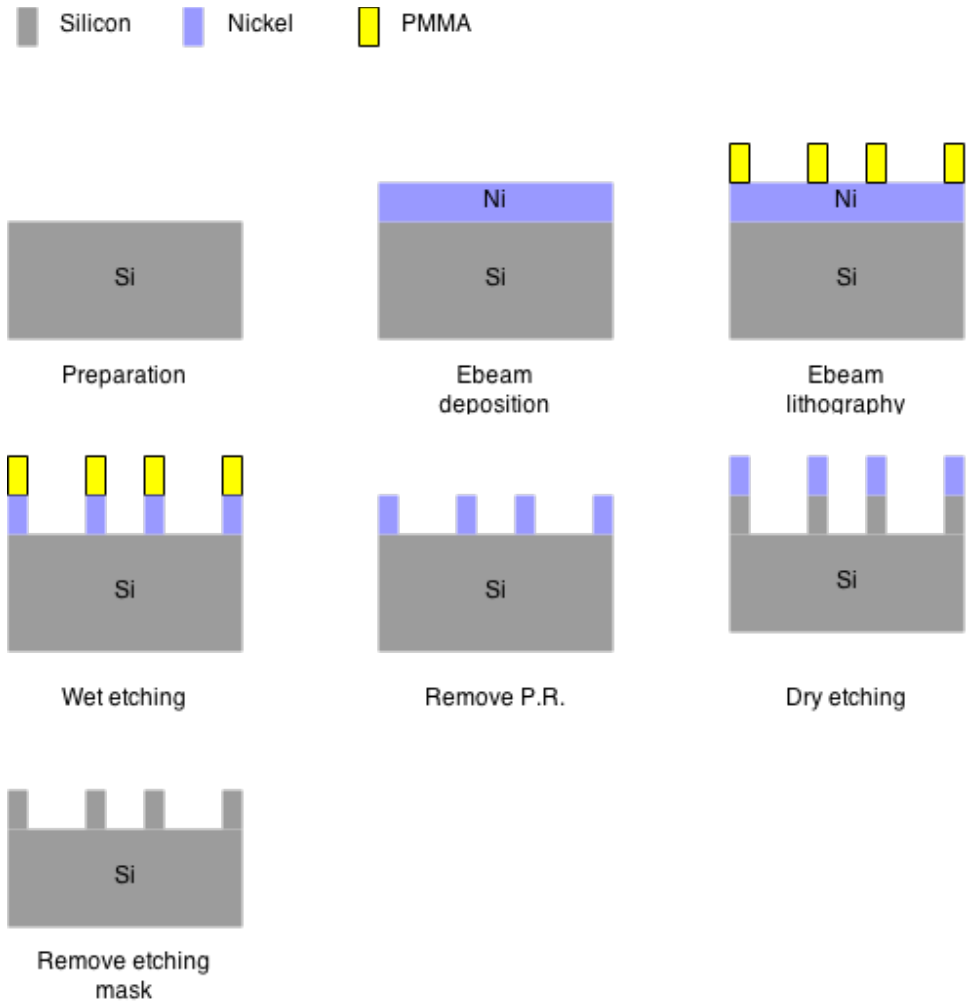

Figure 7.6 Mold creation process flow.

Table 7.3. E-beam Lithography Recipe.

Substrate	25 mm square SOI (220 nm silicon on 3 μm SiO_2)
Photoresist	Hydrogen Silsesquioxane resist (HSQ, Dow-Corning XP-1541-006)
Spin coat	4000 RPM
Soft bake	80 °C, 4 minute
Exposure time	JEOL JBX-6300FS, 100KV, 8nA, machine grid 1 nm, beam stepping grid 6 nm, dose 2800 μC/cm2
Developer	25% Tetramethylammonium hydroxide (TMAH)
Develop time	4 minutes

Table 7.4. Dry Etching Recipe.

Method	ICP
Gas	Chlorine
Pressure	12 mT
Power	800 W
Bias	40 W
Plat temperature	20 degree C
Bias voltage	185 V
Adhesion	Perfluoropolyether vacuum oil

According to the literature, the printing recipe is 4000 psi at 120 ˚C for 300 seconds [60]. The transition temperature of SU-8 is greater than 200 ˚C [61]. This value is 80 ˚C higher than the mentioned imprinting temperature. Therefore, SU-8 is considered sustainable under printing process. A fabrication process based on the mold imprinting to transfer patterns is outlined as Figure 7.7.

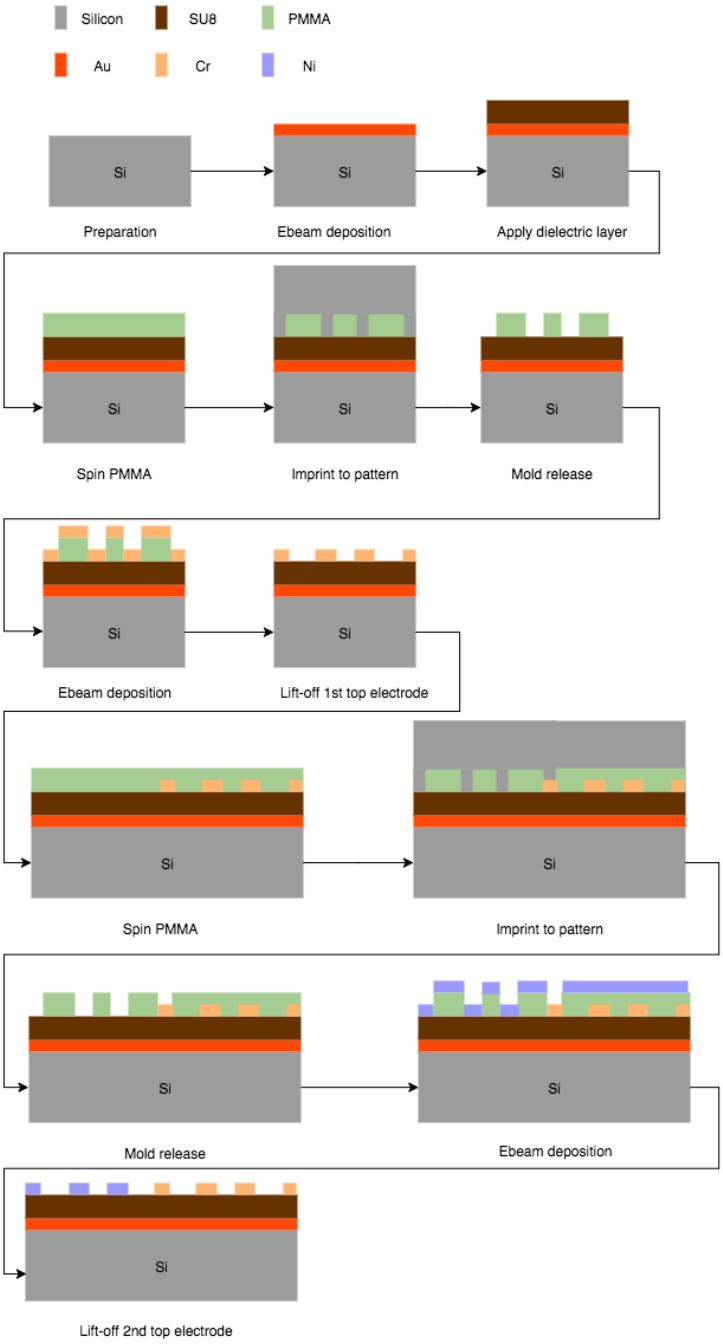

Figure 7.7 The pattern transferring by silicon mold.

Besides the self-developed fabrication processes, the CMOS layered structure is considered as another platform. A CMOS-MEMS thermoelectric micro generator was reported to utilize doped silicon layers as thermoelectric materials [25]. An example of CMOS structures is demonstrated in Figure 7.8 [62].

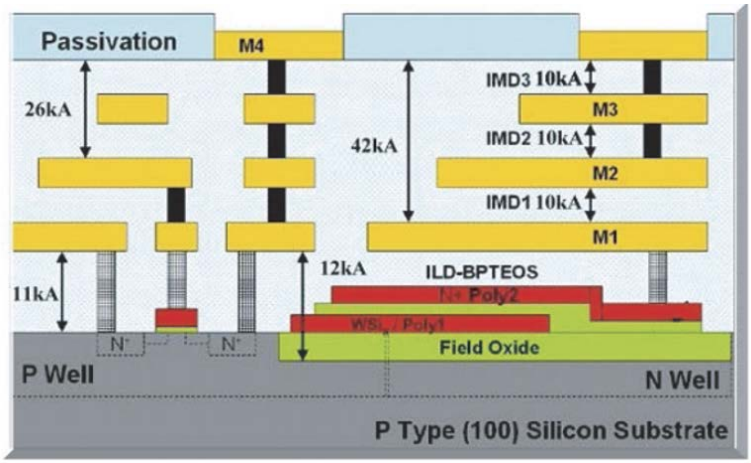

Figure 7.8 A CMOS structure example: TSMC 2P4M process [62].

The doped silicon is the bottom layer of this kind of processes. To utilize this layer as a thermoelectric generator, the substrate can be thinned through appropriate process, for example, chemical mechanical polishing (CMP), wet etching or dry etching. Some metal layers can be combined as bottom electrode and the top passivation layer is preserved for protection. The idea is outlined in Figure 7.9.

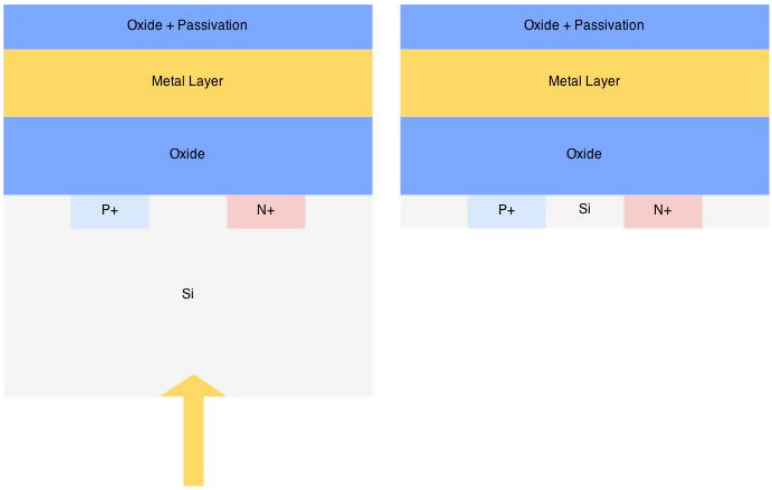

Figure 7.9 The reverse chip by CMOS post-processing.

BIBLIOGRAPHY

[1] United Nations, "Report of the world comission on environment and development: our common future," 1987.

[2] International Energy Agency, "Monthly electricity statistics," International Energy Agency, Paris,2013.

[3] European Commission, "Energy roadmap 2050," ed. Luxembourg: Publications Office of the European Union, 2012.

[4] J. W. Matiko, *et al.*, "Review of the application of energy harvesting in buildings," *Measurement Science and Technology,* vol. 25, p. 012002, 2014.

[5] William C. Brown, *et al.*, "Microwave to DC converter," United States of America Patent, 1969.

[6] Andre Kurs, *et al.*, "Wireless power transfer via strongly coupled magnetic resonances," *Science,* vol. 317, pp. 83-86, 2007.

[7] C. Wu, *et al.*, "Metamaterial-based integrated plasmonic absorber/emitter for solar thermo-photovoltaic systems," *Journal of Optics,* vol. 14, p. 024005, 2012.

[8] LiangKui Sun, *et al.*, "Broadband metamaterial absorber based on coupling resistive frequency selective surface," *Optics Express,* vol. 20, pp. 4675-4680, 2012.

[9] Kamil Boratay Alici, *et al.*, "Optically thin composite resonant absorber at the near-infrared band: a polarization independent and spectrally broadband configuration," *Optics Express,* vol. 19, pp. 14260-14267, 2011.

[10] Harry A. Atwater and A. Polman, "Plasmonics for improved photovoltaic devices," *Nature Materials,* vol. 9, pp. 205-213, 2010.

[11] E. Petryayeva and U. J. Krull, "Localized surface plasmon resonance: nanostructures, bioassays and biosensing—A review," *Analytica Chimica Acta,* vol. 706, pp. 8-24, 2011.

[12] Imogen M. Pryce, *et al.*, "Plasmonic nanoparticle enhanced photocurrent in GaN/InGaN/GaN quantum well solar cells," *Applied Physics Letters,* vol. 96, 2010.

[13] Seok-Soon Kim, *et al.*, "Plasmon enhanced performance of organic solar cells using electrodeposited Ag nanoparticles," *Applied Physics Letters,* vol. 93, 2008.

[14] Kamil Boratay Alici and E. Ozbay, "Photonic metamaterial absorber designs for infrared solar-cell applications," in *Next Generation (Nano) Photonic and Cell Technologies for Solar Energy Conversion*, 2010.

[15] Sachit Grover, *et al.*, "Traveling-wave metal/insulator/metal diodes for improved infrared bandwidth and efficiency of antenna-coupled rectifiers," *IEEE Transactions on Nanotechnology,* vol. 9, 2010.

[16] N. M. Miskovsky, *et al.*, "Nanoscale devices for rectification of high frequency radiation from the infrared through the visible: a new approach," *Journal of Nanotechnology,* vol. 2012, p. 512379, 2012.

[17] O. M. Ramahi, *et al.*, "Metamaterial particles for electromagnetic energy harvesting," *Applied Physics Letters,* vol. 101, p. 173903, 2012.

[18] Frank P. Incropera, *et al.*, *Fundamentals of Heat and Mass Transfer*, 6th ed. Hoboken, New Jersey: John Wiley & Sons, Inc, 2007.

[19] K. N. Liou, *An Introduction to Atmospheric Radiation*. San Diego, CA, USA: Elsevier Science, 2002.

[20] T. J. Seebeck, "Magnetische Polarisation der Metalle und Erze durch Temperatur-Differenz," *Abhandlungen der Königlichen Akademie der Wissenschaften,* pp. 265-373, 1825.
[21] G. J. Snyder, "Small thermoelectric generators," *Interface,* vol. 17, 2008.
[22] D. M. Rowe, *CRC Handbook of Thermoelectrics* Boca Raton, Florida CRC Press, Inc. , 1995.
[23] M. Kishi, *et al.*, "Micro-thermoelectric modules and their application to wrist watches as an energy source," in *18th International Conference on Thermoelectric* 1999.
[24] S.C. Allison, *et al.*, "A bulk micromachined silicon thermopile with high sensitivity " *Sensors and Actuators A,* vol. 104, pp. 32-39, 2003.
[25] P.-H. Kao, *et al.*, "Fabrication and characterization of CMOS-MEMS thermoelectric micro generators," *Sensors,* vol. 10, pp. 1315-1325, 2010.
[26] Min Chen, *et al.*, "Numerical modeling of thermoelectric generators with varing material properties in a circuit simulator," *IEEE Transactions on Energy Conversion,* vol. 24, pp. 112 - 124, 2009.
[27] Raşit Ahıska and H. Mamur, "A review: thermoelectric generators in renewable energy," *International Journal of Renewable Energy Research,* vol. 4, pp. 128-136, 2014.
[28] Shuzo Murakamin, *et al.*, "Combined simulation of airflow, radiation and moisture transport for heat release from a human body," *Building and Environment,* vol. 35, pp. 489-500, 2000.
[29] D. J. Griffiths, *Introduction to Electrodynamics,* 3rd ed. New Jersey: Prentice-Hall International 1999.
[30] K. S. YEE, "Numerical solution of initial boundary value problems involving maxwell's equations in Isotropic media," *Antennas and Propagation, IEEE Transactions on,* vol. 14, pp. 302 - 307, 1966.
[31] Yang Hao and R. Mittra, *FDTD Modeling of Metamaterials: Theory and Applications*: Artech House, 2008.
[32] J.-P. Berenger, "Three-Dimensional perfectly matched layer for the absorption of electromagnetic waves," *Journal of Computational Physics,* vol. 127, pp. 363-379, 1996.
[33] S. D. Gedney, "An Anisotropic Perfectly Matched Layer-Absorbing Medium for the Truncation of FDTD Lattices," *IEEE Transactions on Antennas and Propagation,* vol. 44, 1996.
[34] V. A. Soifer, *Diffractive Nanophotonics*. Boca Raton, Florida CRC Press, Inc. , 2014.
[35] J.-L. Lai, *et al.*, "Using an SU-8 photoresist structure and cytochrome C thin film sensing material for a microbolometer," *Sensors,* vol. 12, pp. 16390-16403, 2012.
[36] Ayad Ghannam, *et al.*, "Dielectric microwave Characterization of the SU-8 thick resin used in an above IC process," in *European Microwave Conference 2009,* Rome, Italy, 2009, pp. 1041-1044.
[37] Charlie H. Smith III, *et al.*, "SU-8 micromachining of millimeter and submillimeter waveguide circuits " in *IEEE MTT-S International Microwave,* 2009.
[38] Cheng-Ling Chang, *et al.*, "Tunable terahertz fishnet metamaterial," *Applied Physics Letters,* vol. 102, p. 151903, 2013.
[39] P. Ding, *et al.*, "Numerical simulations of terahertz double-negative metamaterial with isotropic-like fishnet structure," *Photonics and Nanostructures- Fundamentals and Applications,* vol. 7, pp. 92-100, 2009.

[40] Aleksandar D. Rakić, *et al.*, "Optical properties of metallic films for vertical-cavity optoelectronic devices," *Applied Optics,* vol. 37, pp. 5271-5283, 1998.
[41] Claire M. Watts, *et al.*, "Metamaterial electromagnetic wave absorbers," *Advanced Materials,* vol. 24, pp. 98-120, 2012.
[42] B. A. Munk, *Frequency Selective Surfaces: Theory and Design*. Hoboken, New Jersey: John Wiley & Sons, 2005.
[43] P. K. Singh, *et al.*, "Single and dual band 77/95/110 GHz metamaterial absorbers on flexible polyimide substrate," *Applied Physics Letters,* vol. 99, p. 264101, 2011.
[44] Jodie M. Bell and M. F. Iskander, "A low-profile archimedean spiral antenna using an EBG ground plane," *IEEE Antennas and Wireless Propagation Letters,* vol. 3, pp. 223-226, 2004.
[45] Saniya LeBlanc, *et al.*, "Material and manufacturing cost considerations for thermoelectrics," *Renewable and Sustainable Energy Reviews,* vol. 32, pp. 313-327, 2014.
[46] NASA/Goddard Space Flight Center Scientific Visualization Studio. (2001, May 25 2015). *Terra/CERES View of the Earth*. Available: http://svs.gsfc.nasa.gov/cgi-bin/details.cgi?aid=2328
[47] L. D. Landau and E. M. Lifshitz, *Electrodynamics of Continuous Mediea*. New York: Pergamon Press Inc, 1984.
[48] Jingbo Sun, *et al.*, "An extremely broad band metamaterial absorber based on destructive interference," *Optics Express,* vol. 19, pp. 21155-21162, 2011.
[49] J. K. Gansel, *et al.*, "Gold helix photonic metamaterial as broadband circular polarizer," *Science,* vol. 325, pp. 1513-1515, 2009.
[50] Frank L. Pedrotti, *et al.*, *Introduction to Optics*, 3rd ed.: Pearson Education Limited, 2007.
[51] H.-R. Lin and W.-C. Wang, "Energy dissipation of electromagnetic absrober in terahertz gap," presented at the 2014 International Congerence on Optomechatronic Technologies, Seattle 2014.
[52] Fan Zhang, *et al.*, "Design of a 300-mV 2.4-GHz Receiver Using Transformer-Coupled Techniques," *IEEE JOURNAL OF SOLID-STATE CIRCUITS,* vol. 48, pp. 3190 - 3205, 2013.
[53] G. Jeffrey Snyder and E. S. Toberer, "Complex thermoelectric materials " *Nature Materials,* vol. 7, pp. 105-114, 2008.
[54] C. Goupil, *et al.*, "Thermodynamics of Thermoelectric Phenomena and Applications," *Entropy,* vol. 13, pp. 1481-1517, 2011.
[55] N. Ghafouri, "Bismuth Telluride and Antimony Telluride Based Co-evaporated Thermoelectric Thin Films: Technology, Characterization, and Optimization," Doctor of Philosophy Electrical Engineering The University of Michigan, Ann Harbor, 2012.
[56] Peter Markos and C. M. Soukoulis, *Wave Propagation: From Electrons to Photonic Crystals and Left-Handed Materials*: Princeton University Press 2008.
[57] E. W. Marchand, *Gradient Index Optics*. New York, New York: Academic Press Inc., 1978.
[58] C. Vieu, *et al.*, "Electron beam lithography: resolution limits and applications," *Applied Surface Science,* vol. 164, pp. 111-117, 2000.

[59] Yun Wang, *et al.*, "Focusing sub-wavelength grating couplers with low back reflections for rapid prototyping of silicon photonic circuits," *Optics Express*, vol. 22, pp. 20652-20662, 2014.
[60] Sunghoon Kwon, *et al.*, "Fabrication of Metallic Nanodots in Large-Area Arrays by Mold-to-Mold Cross Imprinting (MTMCI)," *Nano Letters*, vol. 5, pp. 2557-2562, 2005.
[61] W. H. Teh, *et al.*, "Effect of low numerical-aperture femtosecond two-photon absorption on (SU-8) resist for ultrahigh-aspect-ratio microstereolithography," *Journal of Applied Physics*, vol. 97, p. 054907, 2005.
[62] Chun-Chieh Wang, *et al.*, "An optimal design of thermal-actuated and piezoresistive-sensed CMOS-MEMS resonant sensor," *Journal of Micromechanics and Microengineering*, vol. 23, 2013.
[63] Ellen J. Zeman and G. C. Schatz, "An accurate electromagnetic theory study of surface enhancement factors for Ag, Au, Cu, Li, Na, Ga, In, Zn, and Cd " *Journal of Physical Chemistry* vol. 1987, pp. 634-643, 1986.
[64] Dominique Barchiesi and T. Grosges, "Fitting the optical constants of gold, silver, chromium, titanium, and aluminum in the visible bandwidth," *Journal of Nanophotonics*, vol. 8, p. 083097, 2014.
[65] J. W. Cleary, *et al.*, "IR permittivities for silicides and doped silicon " *Journal of the Optical Society of America B* vol. 27, pp. 730-734, 2010.
[66] D. R. Lide, *CRC Handbook of Chemistry and Physics, Internet Version 2005*. Boca Raton, Florida CRC Press, Inc. , 2005.
[67] James F. Shackelford and W. Alexander, *CRC Material Science and Engineering Handbook*. Boca Raton, Florida CRC Press, Inc. , 2001.
[68] A. Graf, *et al.*, "Review of micromachined thermopiles for infrared detection," *Measurement Science and Technology*, vol. 18, pp. R59-R75, 2007.
[69] P. E. Hopkins and L. M. Phinney, "Thermal conductivity measurements on polycrystalline silicon microbridges using the 3ω Technique," *Journal of Heat Transfer*, vol. 131, p. 043201, 2009.

APPENDIX A

Drude Model and Drude-Lorentz Model

When operation frequency is approaching the infrared region, the Drude model is used for modeling of material properties. The Drude model equation for frequency dependent permittivity is

$$\varepsilon(\omega) = 1 - \frac{\omega_p^2}{\omega^2 + i\omega\Gamma}.$$

Even in the study of terahertz metamaterials, the importance of the Drude model for gold electrodes has been emphasized [39]. The plasma frequency and oscillation frequency are key parameters to model gold as a single-negative dielectric material. Some other materials have similar properties and Table A-1 lists key parameters for few common conductors.

Table A-1 Drude Model Parameters

	Collision frequency: Γ (1/s)	Plasma frequency: ω_p (rad/s)
Au [63]	1.71×10^{13}	1.37×10^{16}
Al [64]	7.56×10^{14}	3.92×10^{16}
Cr [64]	4.10×10^{14}	1.59×10^{16}
Ni [40]	1.16×10^{13}	2.42×10^{16}
Poly Silicon (P-type) [65]	$1.6.93 \times 10^{12}$	2.13×10^{14}
Poly Silicon (N-type) [65]	8.95×10^{12}	5.47×10^{13}

Different from the Drude model, the Drude-Lorentz model includes the intra-band electron transition of metals [40]. Though the operation frequency of the presented devices may not reach that high of frequency, the Drude-Lorentz model provides a reference for rarely seen chromium and nickel. The following figures show two curves to model the imaginary and real parts of nickel and chromium, respectively.

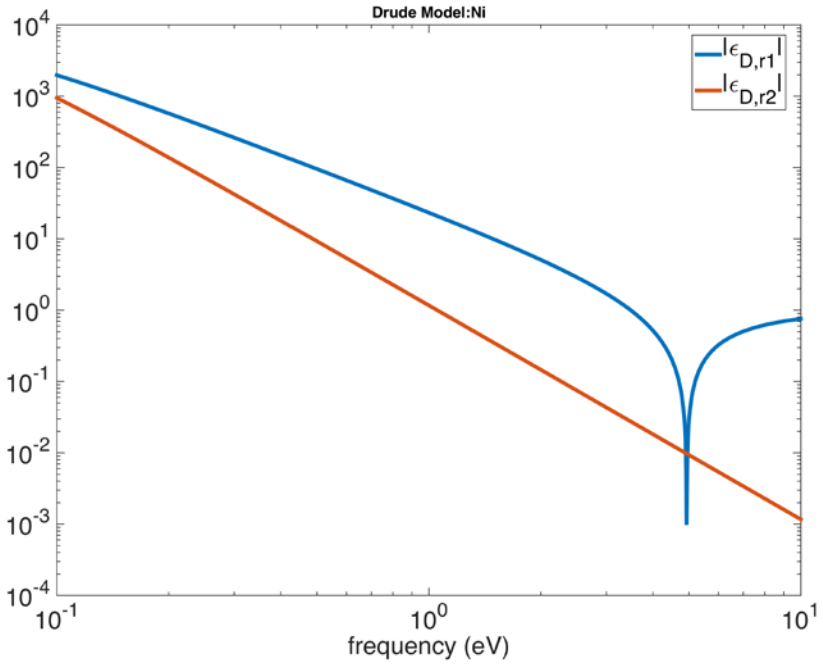

Figure A-1 Log-log scale Drude-Lorentz model of nickel. The blue line is the real part and red line is the imaginary part.

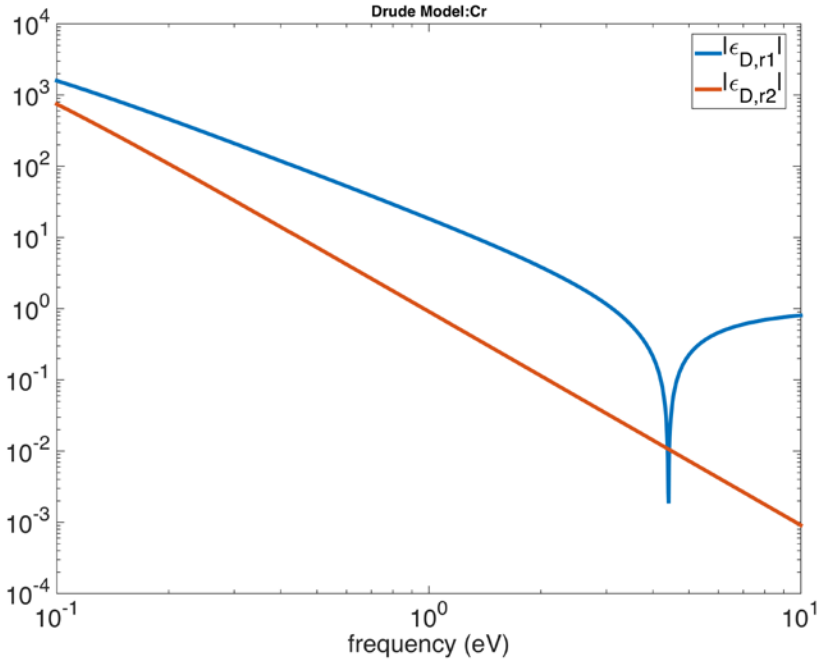

Figure A-2 Log-log scale Drude-Lorentz model of chromium. The blue line is the real part and red line is the imaginary part.

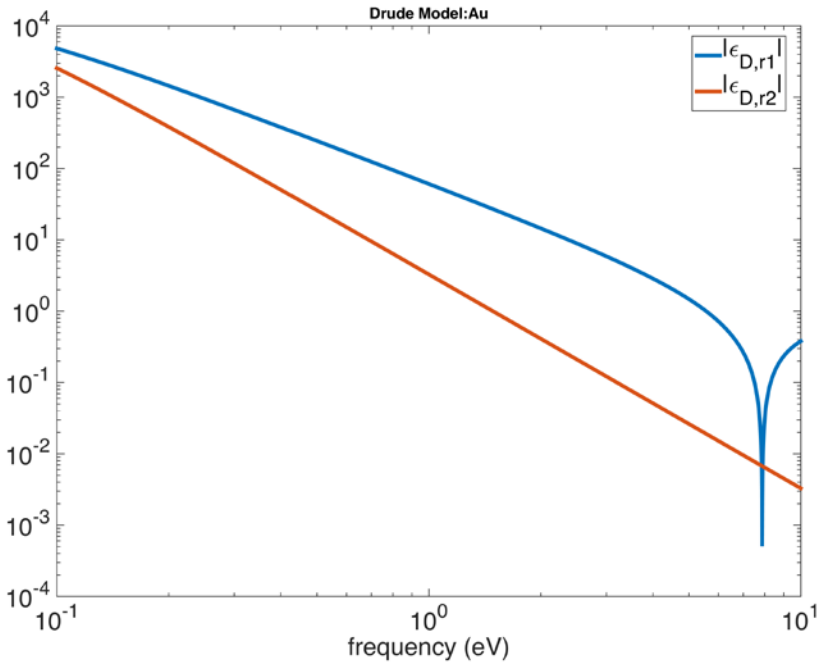

Figure A-3 Log-log scale Drude-Lorentz model of gold. The blue line is the real part and red line is the imaginary part.

Thermal Material Properties and Seebeck Coefficient

Reviewing the heat diffusion equation, the transient term is now removed and the problem is simplified to

$$\nabla^2 T + \frac{\dot{q}}{k} = 0$$

Once the energy dissipation is evaluated after electromagnetic simulation, it can be substituted into the heat diffusion equation and the temperature field can be solved for. The conductivity, heat capacity, density and derived heat diffusivity are important parameters in thermal analysis. Thermal properties of some materials are listed in Table A-2 [66-68].

Table A-2 Table of Material Thermal Properties.

	Density (kg/m^3)	Thermal conductivity (W/k/m)	Heat capacity (KJ/K/Kg)	Thermal diffusivity (m^2/s)	Seebeck coefficient (μV/K)
Au	19.28×10^3	318	0.13	1.27×10^{-4}	1.94
Cr	7.19×10^3	93.9	0.45	2.90×10^{-5}	21.8
Ni	8.91×10^3	90.9	0.44	2.32×10^{-5}	-19.5
Ti	4.506×10^4	21.9	0.53	9.17×10^{-6}	
SU8	1190	0.2	1.20 [35]	1.40×10^{-7}	
SiO_2	2200	1.42 [25]	0.75 [66]	8.61×10^{-7}	
Poly-Si	2700[69]	32 [25]	0.75	1.8×10^{-5}	450+5.28 (p-type) -450+5.28 (n-type) [24]
Air	1.2041	0.0257	1.01	2.11×10^{-5}	

APPENDIX B

A Case Study of Voltage Generation at Different Wavelengths

The voltage generation at 30 THz has been described in section 4.3. Specifically, the voltage outputs of an 11-by-11 array at 30 THz are demonstrated on Figure 4.28. Some different cases are tested in this section.

According to the Wien's displacement law [18], the wavelength can be derived from the object temperature. Given an offset temperature, for example, a normal temperature at 10 ºC in autumn, the operation wavelength is 10.23 μm. The operation frequency is equivalent to 29 THz. Figure 4.10 shows this frequency is included in the target spectrum and the absorption is close to the value at 30 THz. However, it is noted that the energy dissipation pattern at 29 THz is slightly different from that at 30 THz. The energy dissipated to the left arm more than the 30 THz case. This discovery also suggests the energy dissipation patterns change as the operation frequency shifts. A less temperature difference between spiral center and spiral right or left end is expected due to this extra energy dissipation.

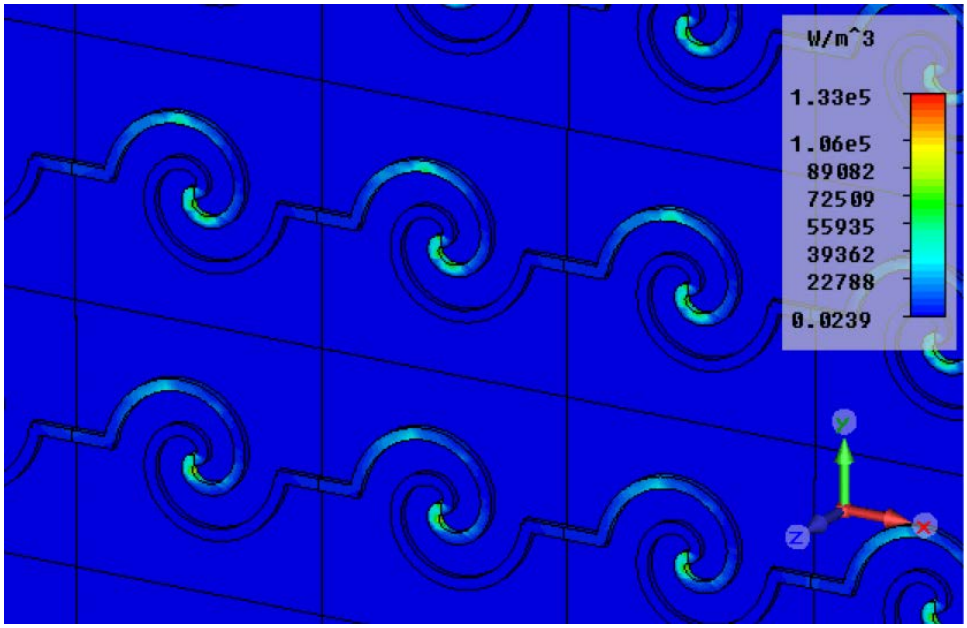

Figure B-1 Electromagnetic energy dissipation over spiral at 30 THz: central part of an 11-by-11 array.

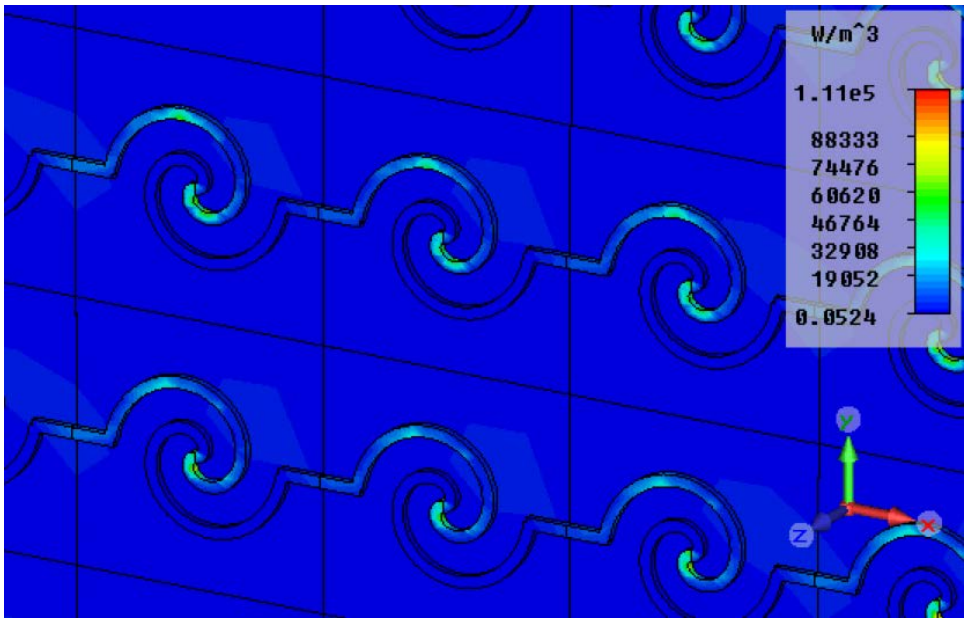

Figure B-2 Electromagnetic energy dissipation over spiral at 29 THz: central part of an 11-by-11 array.

The Figure B-3 shows the temperature distribution at 29 THz. It looks similar to the case of 30 THz. However, The V_{ave} in this case is 131 nV, which is less than the result 174 nV at 30 THz. This outcome matches our prediction: dispersed energy lowers the temperature difference.

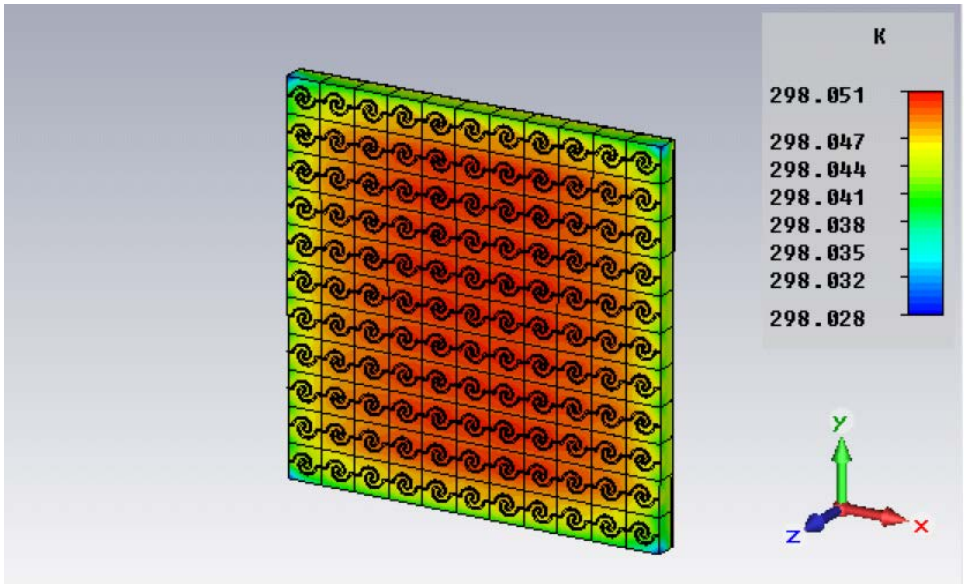

Figure B-3 Temperature distribution of 11-by-11 Fermat spiral design at 29 THz.

Another case is 38.6 THz, which corresponds to 100 ºC. It is noted that this frequency is out of the optimized frequency range. The energy dissipation pattern in Figure B-4 does not suggest concentrated distribution. The Figure B-5 also shows a very uniform temperature

distribution, which is different from the cases of 29 THz and 30 THz. As a result, the V_{ave} in this case is 41.3 nV, which is much less than the value at 30 THz.

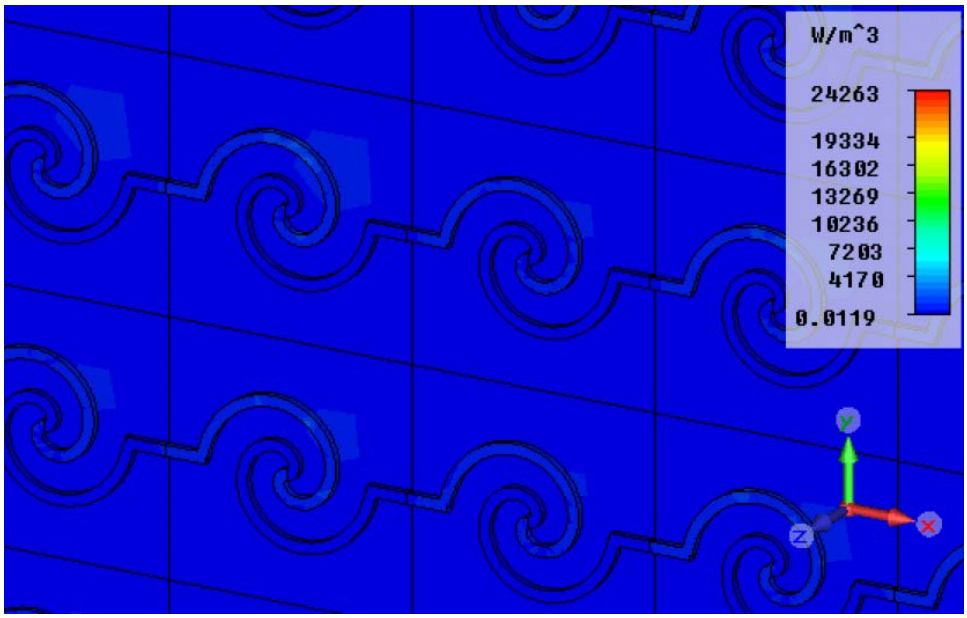

Figure B-4 Electromagnetic energy dissipation over spiral at 38.6 THz: central part of an 11-by-11 array.

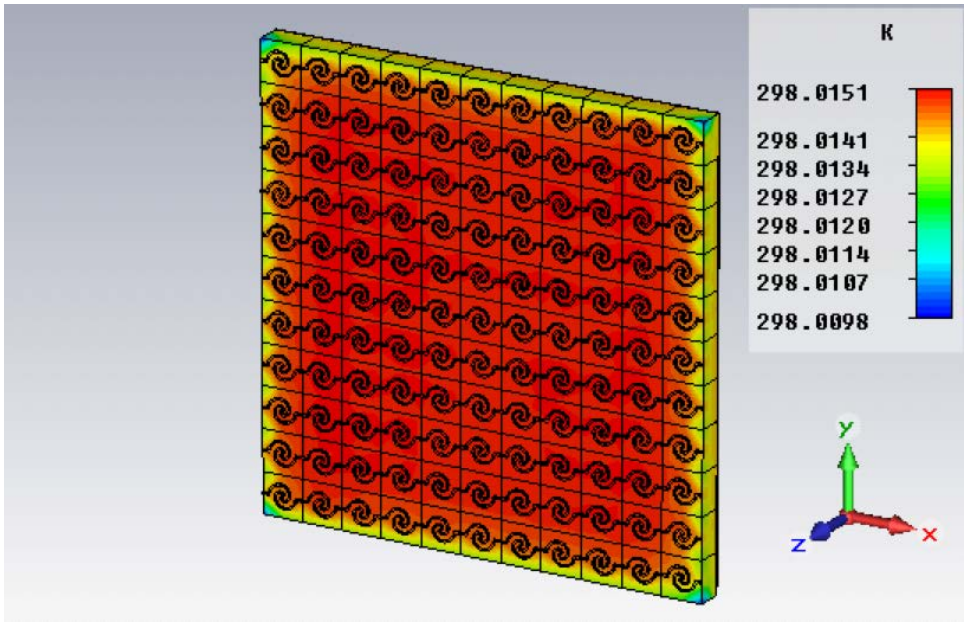

Figure B-5 Temperature distribution of 11-by-11 Fermat spiral design at 38.6 THz.

VITA

Hong-Ren Lin was born in Pingtung, Taiwan. He got a bachelor degree of aeronautics and astronautics engineering from National Cheng Kung University (2004) and a master degree of applied mechanics from National Taiwan University (2006). He is lucky to have many intelligent friends and mentors who are willing to help him through each transition. He got Ph.D. in mechanical engineering from University of Washington (2015). He is interested in semiconductor and electromagnetic wave.